

**PERFORMANCE OF A SINGLE-ROW HEAT
EXCHANGER AT LOW IN-TUBE FLOW RATES**

A Thesis

Submitted to the Graduate School
of the University of Notre Dame
in Partial Fulfillment of the Requirements
for the Degree of

Master of Science
in Mechanical Engineering

by

Xiangwei Zhao, Bachelor of Engr., Master of Engr.

Dr. K.T. Yang, Dr. Mihir Sen, Directors

Department of Aerospace and Mechanical Engineering

Notre Dame, Indiana

April 1995

**PERFORMANCE OF A SINGLE-ROW HEAT EXCHANGER
AT LOW IN-TUBE FLOW RATES**

by

Xiangwei Zhao

Abstract

The steady and time-dependent behavior of a single-row heat exchanger with water and air in the in-tube and over-tube sides has been studied experimentally. A wide range of water flow rates including laminar and turbulent flows was used. Two methods of steady-state data analysis were employed: a least-squares power-law technique to obtain both air- and water-side heat transfer correlations and a neural network technique to model the heat exchanger without use of any correlation. The two methods predict heat exchanger behavior to essentially the same degree of accuracy. The experimental observations are quantitatively compared to the predictions of correlations available in the literature as well as to manufacturer's data. The manufacturer's data do not exist for extremely low flow rates. Furthermore, the experiments show that in this range, a turbulent flow correlation works better than a laminar one, even though the flow is laminar. A simple dynamical model has been developed for the time-dependent response of the heat exchanger. There are two characteristic times, one associated with the hydrodynamics and the other with the thermal processes. The theoretical predictions are found to be in qualitative agreement with experimental data.

TABLE OF CONTENTS

LIST OF SYMBOLS	iii
LIST OF TABLES	vii
LIST OF FIGURES	viii
ACKNOWLEDGMENTS	ix
1 INTRODUCTION	1
1.1 Motivation	1
1.2 Background	2
1.3 Present Work	5
2 TEST FACILITY AND EXPERIMENTS	7
2.1 Introduction	7
2.2 Test Facility	7
2.3 Components of Test System	8
2.3.1 Components of water-side loop	8
2.3.2 Components of wind tunnel	14
2.3.3 Electrical control panel	15
2.3.4 Measuring sensors	15
2.3.5 Data acquisition system	16
2.4 Measuring Parameters	16

2.5	Calibration	18
2.5.1	Calibration of thermocouples	18
2.5.2	Calibration of flow meter	19
2.5.3	Calibration of wind tunnel	19
2.6	Temperature Measurement	23
2.6.1	Air-side temperature measurement	23
2.6.2	Water-side temperature measurement	23
3	DATA ANALYSIS BY LEAST-SQUARES METHOD	27
3.1	Introduction	27
3.2	Background on Data Analysis	28
3.2.1	Extrapolation method	28
3.2.2	Log-mean temperature difference method	28
3.3	Least-Squares Power-Law Method	29
3.4	Results and Discussion	32
3.4.1	Air-side heat transfer	33
3.4.2	Water-side heat transfer	34
3.4.3	Effect of bends on water-side heat transfer	38
3.4.4	Overall heat transfer	40
3.5	Conclusions	40
4	DATA ANALYSIS BY NEURAL NETWORK METHOD	44
4.1	Introduction	44
4.2	Background on Neural Networks	47
4.3	Neural Network Method	51

4.4	Training Results of Neural Network	52
4.5	Prediction Results of Neural Network	54
4.6	Conclusions	61
5	DYNAMICAL MODELING OF HEAT EXCHANGERS	62
5.1	Introduction	62
5.2	Theoretical Model	62
5.3	Experiments	65
5.4	Results and Discussion	66
5.5	Conclusions	70
6	CONCLUSIONS AND RECOMMENDATIONS	71
6.1	Conclusions	71
6.2	Recommendations	72
	BIBLIOGRAPHY	73
	APPENDIX-A: UNCERTAINTY ANALYSIS	76
.1	Error Sources	77
.2	Data Reduction and Uncertainty Analysis	79
.2.1	Curve fitting	79
.2.2	Bias errors due to calibration	80
.2.3	Propagation of uncertainty to results	81
.3	Sample Calculation	83
.3.1	Calibration results	83
.3.2	Calibration error	84
.3.3	Precision error	85

.3.4	Uncertainty in heat transfer	85
	APPENDIX-B: LEAST-SQUARES APPROACH	87
	APPENDIX-C: FORTRAN CODE	89

LIST OF SYMBOLS

English

A	Y intercept constant for linear function
A_a	air-side total area = $A_f + A_t$
A_f	total surface area of fin
A_{fr}	frontal area of heat exchanger
A_t	outside surface area of bare heat exchanger tube
A_w	water-side heat transfer area
a	dimensionless constant, or intercept constant for linear function
B	bias error
b	dimensionless constant
c_p	specific heat at constant pressure
D_i	inner diameter of the coil tube
F	flow rate
f	sigmoid function
f'	derivative of sigmoid function
f_d	fan driving frequency
f_w	friction factor in tube
H	wind tunnel's height
h	convective heat transfer coefficient
j	Colburn j -factor, $Nu/(RePr^{1/3})$
k	thermal conductivity

L	total length of the coiled tube
L_s	straight tube length between two nearest bends
l	effective tube length
M	slope
m	dimensionless constant, slope
Nu	Nusselt number
n	dimensionless constant
P	pressure
Pr	Prandtl number
p	Perimeter (A_a/L)
$Q, Q(t)$	heat transfer rate
R	thermal resistance
R_c	radius of curvature of bend
Re	Reynolds number
r	parameter, defined by eqn (.18)
S	precision error
s	activation of neural node
T	temperature
t	time, target output of neural network
U	overall heat transfer coefficient
U_r	uncertainty in parameter r
V	fluid velocity, sensor's voltage output
W	wind tunnel's width
w	weight

x	neural node input
y	neural node output

Greek

β	parameter, defined by eqn (5.2)
γ	correlation coefficient
Δ	change
δ	fin spacing of the test heat exchanger
ϵ	error
η	total efficiency of air-side surface
η_0	fin efficiency
θ	non-dimensional temperature, sensitivity
μ	dynamical viscosity
μ_b	dynamic viscosity evaluated at bulk temperature
μ_s	dynamic viscosity evaluated at tube wall temperature
ν	kinematic viscosity
ν_r	degrees of freedom
ξ	learning rate
ρ	density
τ_α	time constant

Subscripts

a	air side
h	horizontal direction
i, j	neural node number
in	inlet
o	outer
out	outlet
s	steady state
v	vertical direction
w	water side
0	initial
∞	ambient condition

LIST OF TABLES

2.1	Ranges of Experimental Parameters	17
2.2	Temperature ($^{\circ}\text{C}$) at inlet region	24
2.3	Temperature ($^{\circ}\text{C}$) at outlet region	25
4.1	Testing Data	57

LIST OF FIGURES

2.1	Schematic of test facility 1. blower 2. flow straightener 3. heating coil 4. pitot-static tube 5. screen 6. thermocouple 7. differential pressure gauge 8. motor 9. electrical heater 10. water pump 11. strainer 12. flow meter 13. valve	9
2.2	Front view of test facility	10
2.3	Side view of test facility	11
2.4	Back view of test facility	12
2.5	View of water-side loop	14
2.6	Schematic of thermocouple calibration	19
2.7	Calibration result for thermocouple 1	20
2.8	Schematic for calibration of flow meter	20
2.9	Flow meter calibration result	21
2.10	Velocity distribution along the horizontal and vertical centerlines of the wind tunnel	22
2.11	Wind tunnel calibration result	22
2.12	Inlet and outlet sections	25
3.1	Schematic model of cross-flow heat exchanger	29
3.2	Air-side Nusselt number	35

3.3	Air-side heat transfer coefficients, compared to extrapolation method result	35
3.4	Water-side heat transfer correlation, compared to straight tube correlations	37
3.5	Effect of bends on water-side Nusselt number	41
3.6	Comparison of experimental data with power-law least-square results	41
3.7	Heat transfer rate for $V_a = 1.31$ m/s, $T_{w,in} \approx 54.0^\circ\text{C}$, $T_{a,in} \approx 21.0^\circ\text{C}$	42
3.8	Heat transfer rate for $V_a = 1.90$ m/s, $T_{w,in} \approx 54.0^\circ\text{C}$, $T_{a,in} \approx 21.0^\circ\text{C}$	42
4.1	Configuration of a simple neural network	49
4.2	Typical model of a single node	49
4.3	Sigmoid function and its derivative	50
4.4	Neural network configuration used for modelling heat exchanger	52
4.5	Errors of neural network via learning cycle number during train- ing process	55
4.6	Heat transfer rates via water Reynolds number, $T_{w,in} \approx 54.4^\circ\text{C}$, data were used for obtaining correlations and training neural net- work	55
4.7	Air temperature increase via water Reynolds number, $T_{w,in} \approx$ 54.4°C , data were used for obtaining correlations and training neural network	56
4.8	Water temperature drop via water Reynolds number, $T_{w,in} \approx$ 54.4°C , data were used for obtaining correlations and training neural network	56

4.9	Air temperature increase via water Reynolds number, $T_{w,in} \approx 48.9^\circ\text{C}$, new data are used here for comparison	58
4.10	Air temperature increase via water Reynolds number, $T_{w,in} \approx 60.0^\circ\text{C}$, new data are used here for comparison	58
4.11	Water temperature drop via water Reynolds number, $T_{w,in} \approx 48.9^\circ\text{C}$, new data are used here for comparison	59
4.12	Water temperature drop via water Reynolds number, $T_{w,in} \approx 60.0^\circ\text{C}$, new data are used here for comparison	59
4.13	Heat transfer rates via water Reynolds number, $T_{w,in} \approx 48.9^\circ\text{C}$, new data are used here for comparison	60
4.14	Heat transfer rates via water Reynolds number, $T_{w,in} \approx 60.0^\circ\text{C}$, new data are used here for comparison	60
5.1	Variation of air-side outlet temperature with time, $F_w = 0.39$ gpm, $T_{w,0} = T_\infty$	67
5.2	Variation of air-side outlet temperature with time, $F_w = 0.44$ gpm, $T_{w,0} = T_\infty$	68
5.3	Variation of air-side outlet temperature with time, $F_w = 0.66$ gpm, $T_{w,0} = T_\infty$	68
5.4	Variation of water-side outlet temperature with time, $T_{w,0} = T_\infty$	69
5.5	Air-side outlet temperature variation with time, $T_{w,0} - T_\infty = 10^\circ\text{C}$	69
.1	Schematic of uncertainty analysis	78

ACKNOWLEDGMENT

I would like to thank my advisors, Dr. K.T. Yang and Dr. Mihir Sen, for providing constant encouragement, help, guidance, and suggestions throughout my study at the University of Notre Dame. I also wish to thank Dr Samuel Paolucci and Dr. Joseph M. Powers for their interest as thesis readers

I wish to express my sincere thanks to Mr. Rodney L. McClain for his valuable help and discussion through this research project.

I would also like to thank Kevin Peters for his help with the data acquisition systems.

I appreciate Ricardo Romero-Mendez for his help on part of the experiments.

Finally, I gratefully acknowledge the interest and support of D. K. Dorini and BRDG-TNDR.

CHAPTER 1

INTRODUCTION

1.1 Motivation

A heat exchanger coil is a device which provides for transfer of thermal energy between fluids at different temperatures. Heat exchanger coils are important in an extremely wide range of industrial applications, such as in the areas of process, power, automotive, air conditioning, refrigeration, cryogenics, heat recovery, and manufacturing industries.

Typically, such coils operate at full load with water-side velocities in the range of fully developed turbulent flow. However, under partial load conditions, as well as in such coil systems as those employing thermal storage units, tube-side water velocities can become much lower. Current procedures for predicting coil performance are suitable for water velocities in fully developed turbulent flow region but become increasingly inaccurate at lower water velocities (Mirth, et al., 1993). Engineers involved with installing heating, ventilating, and air-conditioning (HVAC) systems that require low water velocities in the heat exchanger coil have noted that the coil manufacturer's software often overpredicts

coil performance.

The main objective of this research project is to determine experimentally the performance of heating coils at low and very low water flow rate, which cover both laminar and transitional regions. Such data are critically needed in the hydronics industry to better design hydronic and control systems for optimum energy conservation. In addition to generating steady-state data of coil performance at low Reynolds numbers, another goal of this study is to determine the coil performance responses to transient or dynamic load conditions. Such data are completely lacking at the present time.

1.2 Background

Despite the importance of single-row fin-and-tube heat exchangers, very little experimental work of general use has been reported. The most extensive investigation in this area has been that of Shepherd (1956), who tested a total of 38 different single-row coils. The information is presented in the form of average air-side transfer coefficients and transfer rates. These transfer coefficients were evaluated without the fin efficiency being taken into account. In addition, there is uncertainty in his data reduction procedure. The method used to determine the air-side heat transfer coefficients was to measure the overall thermal resistance and then to extrapolate it for the limit of zero water-side resistance.

A different approach for the calculation of the heat transfer coefficient was that used by Saboya and Sparrow (1974). In their work the analogy between heat and mass transfer was used to obtain local and average transfer coefficients. The mass transfer measurements were performed using the naphthalene subli-

mation technique. These experiments thus correspond to heat transfer from isothermal fins, that is fins with efficiency $\eta = 1$.

A paper by Rich (1973), analyzed the effect of fin spacing on the heat transfer performance on plate fin-and-tube heat exchangers. In the experiment, the fin spacing was varied from zero to 21 fins per inch. In a further paper (Rich, 1975), the effect of number of tube rows was studied. The experiment was made for six plate fin-and-tube heat exchangers in which the primary physical variable was the flow depth, which varied from one to six rows. The heat transfer coefficient was presented using the Colburn j -factor. It is important to mention that the test coils in the experiments were of all-copper construction, and in the data reduction, a fixed average value of metal resistance was used provided that it varies only slightly with the air resistance.

McQuiston (1981) used data from Rich (1975) and from his own experiments to obtain the first correlation for smooth-plate fin and tube coils. He considered the effects of rows, fin pitch, and other geometrical parameters and generalized a heat transfer correlation useful for dry coils. The heat transfer correlation was developed in two steps. The first step developed a correlation for finned-tube geometries having four tube rows

$$j_4 = 0.0014 + 0.2618 Re_a^{-0.4} \left(\frac{A}{A_t} \right)^{-0.15} \quad (1.1)$$

Then a multiplier was considered to account for the effect of the number of rows

$$\frac{j_N}{j_4} = \frac{1 - 1280 N Re_{a,L}^{-1.2}}{1 - 5120 Re_{a,L}^{-1.2}} \quad (1.2)$$

where $500 < Re_a < 24700$. The range of validity of the geometrical parameters is not specified, but is logical to think that it is similar to that of Webb (1986)

below.

Webb (1986) complemented the data used by McQuiston (1981) with data for bundles of finned tubes. He developed his own regression technique to obtain another correlation for plate finned-tube heat exchangers with plain fins. This new correlation predicts the four row j -factor

$$j_4 = 0.14Re_a^{-0.328} \left(\frac{S_t}{S_1}\right)^{-0.502} \left(\frac{s}{D}\right)^{0.0312} \quad (1.3)$$

and then corrects it for the effect of different number of rows

$$\frac{j_N}{j_4} = 0.991[2.24Re_a^{-0.092} \left(\frac{N}{4}\right)^{-0.031}]^{0.0607(4-N)} \quad (1.4)$$

where $2400 < Re_a < 24700$. The range of dimensionless variables for equations (1.2) and (1.4) are $1.97 < S_t/D < 2.55$; $1.70 < S_1/D < 2.58$; $0.08 < s/D < 0.64$; $1 < N < 8$ or more.

The determination of the inner heat transfer coefficient (water-side) is a problem which has received little attention in papers related to fin-tube heat exchangers. In the vast majority of papers related to fin-tube heat exchangers, simple straight-tube correlations are assumed for the water side circuit, thus leading to inaccurate results in the determination of the inner heat transfer coefficient, especially at low Reynolds numbers. A recent paper of Mirth *et al.* (1993) revealed that cooling coils operating at low water-side Reynolds numbers do not perform as predicted by manufacturer's software. Based upon this observation, they suggested that further research is needed to obtain a suitable prediction for coils operating at low Reynolds numbers. This need is aggravated because in the laminar flow region the inner heat transfer coefficient is even more important in the determination of the overall heat transfer coefficient

than for turbulent flows.

On the other hand, it should be noted here that, even though much experimental data and correlations are now available in the literature on fin-tube heat exchangers, these data largely emphasize the air- or gas-side heat transfer characteristics. In the present study, however, the emphasis is placed on the water-side heat transfer, particularly on the behavior at low Reynolds number. Such data, as already mentioned, are currently lacking.

1.3 Present Work

The main phase of this research project covers the experimental study of heat exchanger coils with low water-flow rates. For this purpose and for simplicity we concentrate on single-row heat exchangers as a specific example. Chapter 2 gives detail description of the test facility for experimental study of heat exchanger. This chapter includes a description of the components of the test facility, ranges of test parameters, calibration of sensors and fluid bulk temperature measurement. Chapter 3 presents a data analysis method: the least-squares power-law method that simultaneously gives both water- and air-side power-law heat transfer correlations is developed. Also in this chapter, information relating to the performance of the actual heat exchanger being tested is presented and compared to that deduced from heat transfer correlations in the literature and also manufacturer's specifications. The drawbacks of previous methods of data analysis that use extrapolation or the logarithmic mean temperature difference are pointed out. Definitive results on the single-row heat exchanger tested are presented. Chapter 4 introduces an alternative method of analysis based

on the technique of artificial neural networks. Though presented here only as an alternative, this method has certain characteristics that make it very useful in the analysis of systems about which little or nothing is known *a priori*. It is hoped that this technique will become useful in the future especially in the control of hydronic networks. The results of this method are compared to the previous least-squares power-law technique. Chapter 5 presents a preliminary one-dimensional laminar-flow model to simulate the dynamic response of a heat exchanger under the condition of a suddenly-imposed pressure drop, and the results show a qualitative agreement with the experimental data obtained with a single-row heat exchanger. Chapter 6 is a concluding chapter which summarizes the principal achievements of this research.

CHAPTER 2

TEST FACILITY AND EXPERIMENTS

2.1 Introduction

The intent of this research is to determine the effects of reduced water flow rates on the performance of typical fin-tube heat exchangers in a hydronic system. The water flow varies over a wide range, covering laminar, transitional and turbulent flow regions. The test parameters, mechanical equipment and electrical equipment have to be chosen to fit within the constraints imposed by the test facilities. In the following sections, the test facility and its components will be described in detail.

2.2 Test Facility

The experiments were carried out in a test facility that was specifically designed and constructed for the purpose. A schematic of this facility is shown in Figure 2.1. This test facility includes a wind tunnel, a heating system, a data acquisition system, and an electrical control panel. The wind tunnel can supply a constant velocity air flow. A variable-speed indraft blower is used to draw

air through the tunnel in which the heat exchanger is mounted. The heating system can supply hot water with a set temperature for the tested coil. All of the experimental data are recorded by the data acquisition system. The control panel is used for control of the blower, heating system and pump.

Photographs of this test system in different views are shown in Figures 2.2–2.4 respectively. Figure 2.2 shows the control panel and the data acquisition system in front, with the tunnel behind. Figure 2.3 is a side view which includes the connections to the coil as well as the blower on the extreme right. Figure 2.4 is a view from the other side showing the honeycomb at the inlet of the tunnel; the coil can also be observed between the two sections of the tunnel.

2.3 Components of Test System

The test system includes components of the water-side loop, components of the wind tunnel, an electrical control panel, measuring sensors and the data acquisition system. The specifications of these components are described in the following subsections.

2.3.1 Components of water-side loop

The components in the water-side loop include:

- Heating coil: The heat exchanger chosen for testing was a nominal 18 in.×24 in. water coil¹. The fin spacing of this coil is 2.77 mm (110 fins/foot) and the fin thickness is 0.18 mm (0.0071 in.). The coil type is Sigma Flo which may be described as a corrugated shape with high

¹Type T, Trane Air Conditioning Division, The Trane Company, La Crosse, WI 54601

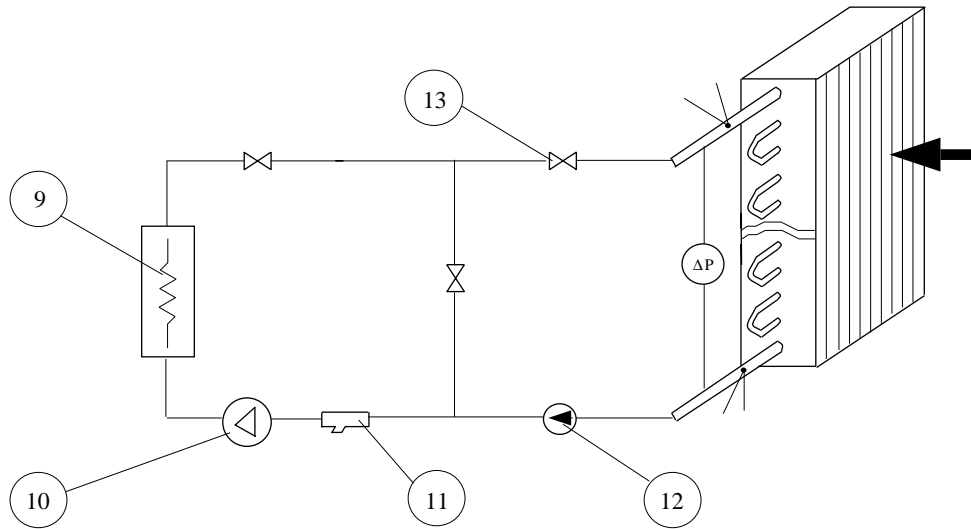
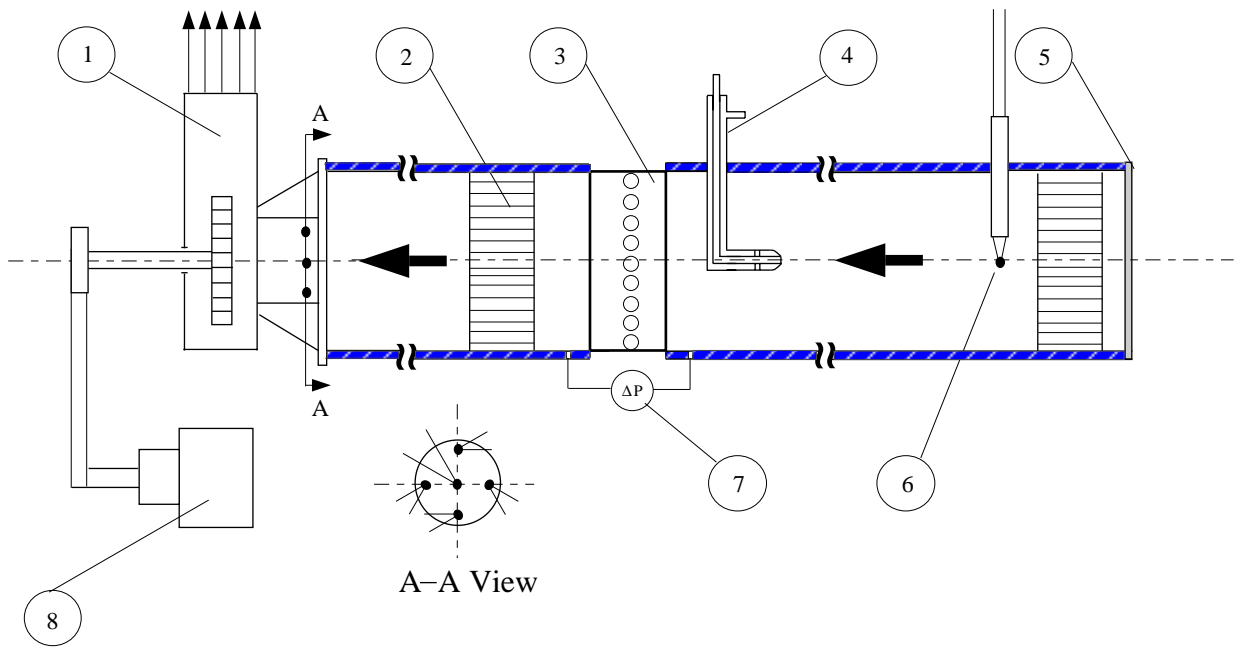


Figure 2.1: Schematic of test facility 1. blower 2. flow straightener 3. heating coil 4. pitot-static tube 5. screen 6. thermocouple 7. differential pressure gauge 8. motor 9. electrical heater 10. water pump 11. strainer 12. flow meter 13. valve

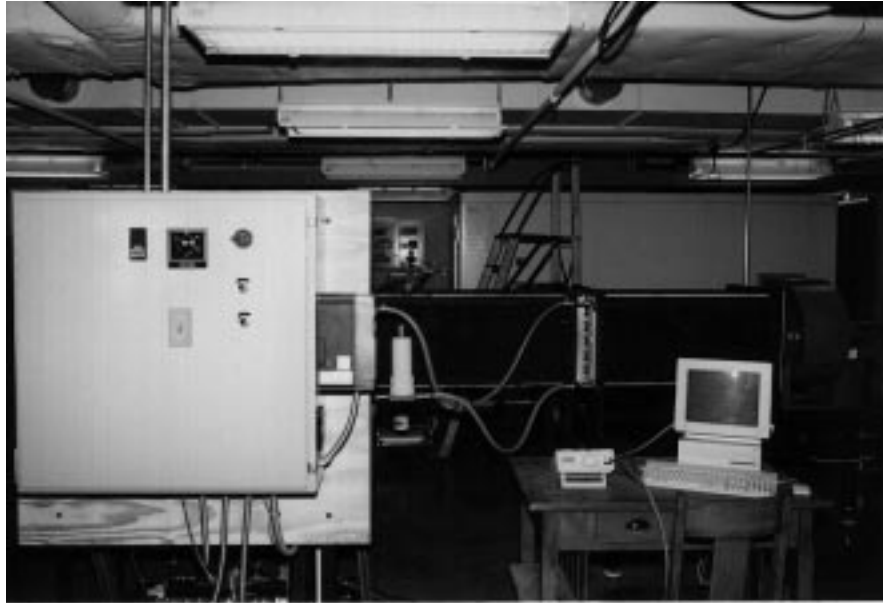


Figure 2.2: Front view of test facility



Figure 2.3: Side view of test facility

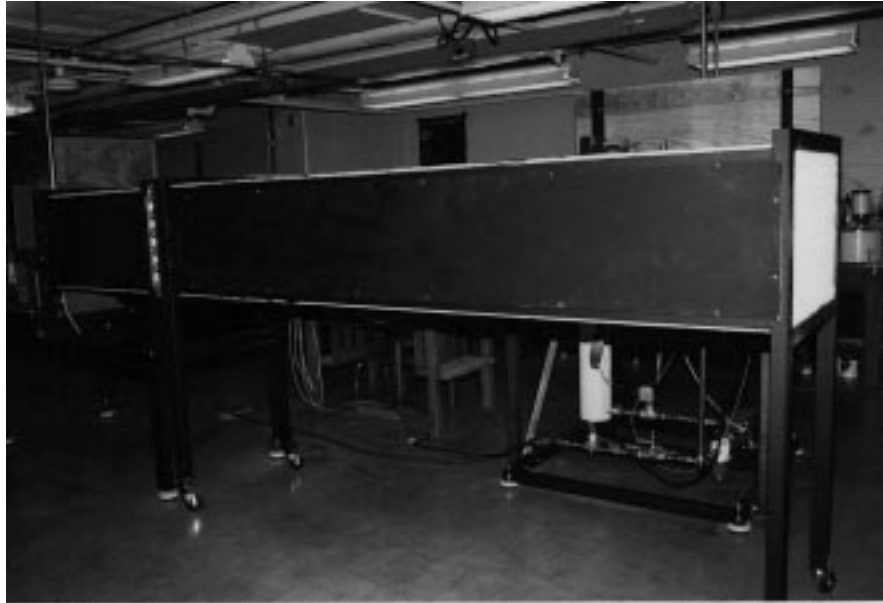


Figure 2.4: Back view of test facility

heat transfer. The specified coil tube has inside and outside diameters of 14.86 mm (0.585 in) and 15.875 mm (0.625 in.), respectively, and makes 12 passes across the heat exchanger's 24 in. dimension. In order to reduce heat loss to the surroundings, the tube bends and metal casing of the coil were insulated using 12.7 mm (1/2 in.) thick foam insulation.

- Water pump²: centrifugal pump, horizontally mounted, with a pumping capacity of 15 – 20gpm.
- Heater: circulation electric heater ³ powered by a 3-phase, 208V, 12KW nominal power supply was chosen.
- Heater temperature controller: PID controller ⁴ to maintain a constant water temperature at the inlet to the heating coil, with a maximum control band width of 1°C.
- Flow control: the flow can be manually controlled using valves.
- Expansion tank: a 2 gallon bladder tank is used to maintain constant pressure at the pump inlet.
- High temperature cut-out switch.
- Low pressure switch.
- Flow switch: this ensures adequate water flow rate.

²W. W. Grainger

³Chromolox

⁴RKC, Rex F400 controller

Figure 2.5 is a photograph which shows some of the details of the above components for the water-side loop. The vertical cylinder is the heater and the pump is located near the floor.

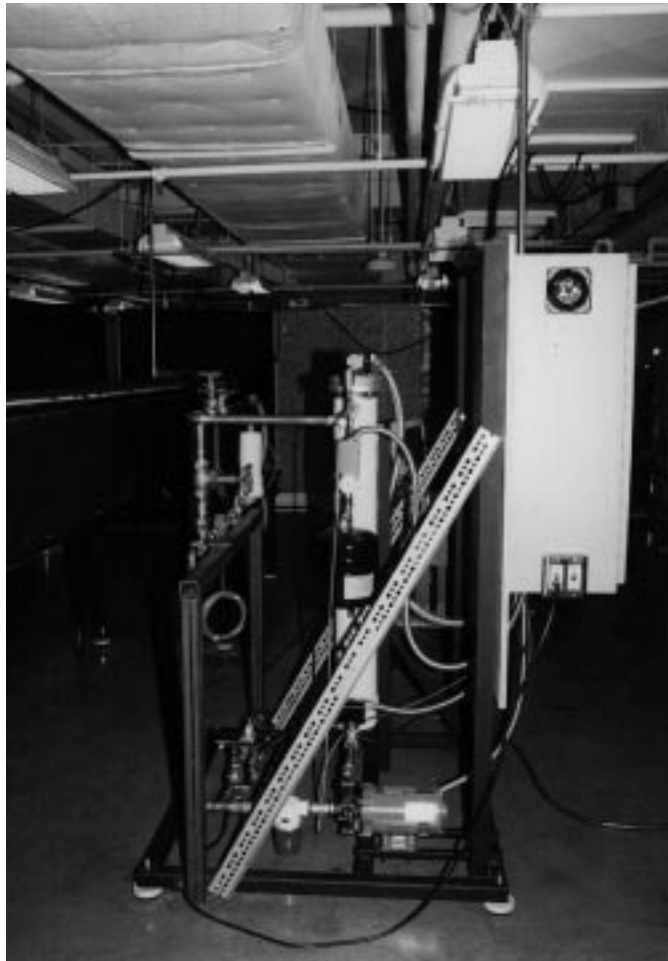


Figure 2.5: View of water-side loop

2.3.2 Components of wind tunnel

The schematic of the wind tunnel is also shown in Figure 2.1. Its components are described in the following:

- A variable-speed blower⁵
- Blower controller: an AC inverter, industrial standard controller⁶ was used for varying the air velocity across the coil
- Flow straightener: industrial packed straw honeycomb bundle (10 in.) was used to ensure a uniform air flow

2.3.3 Electrical control panel

This panel distributes a maximum of 21KVA of three- and single-phase electrical power. It contains the electrical distribution network of all electrical power for the facility and controls for the blower, heater and pump.

2.3.4 Measuring sensors

All of the data in this experiment were measured by the following sensors:

- Flow meter⁷: a turbine flow sensor with a range of 0.2 to 4.5gpm
- Pressure transducer⁸: a differential pressure transducer with a full scale of 0.1 in. water column
- Thermocouple: Type T

⁵New York Blower, Acoustafol PLR

⁶Reliance, GP2000 A-C VS drive

⁷Signet, MK 509-2 Micet

⁸Setra, Model 264

2.3.5 Data acquisition system

A data acquisition/control unit⁹ with 30 channels of differential analog multiplexed input with thermocouple compensation was selected. It has $5\frac{1}{2}$ digit output and $1\ \mu\text{V}$ resolution in the low range of 0–300 mV. A LabVIEW program was written for controlling the data acquisition/control package and carrying on the conversions and data reduction work.

2.4 Measuring Parameters

The measured parameters and their ranges during test were listed below:

- water inlet temperatures $T_{w,in}$: 42.1–65.7°C (107.8°F–150.3°F)
- water outlet temperatures $T_{w,out}$: 22.7–60.2°C (72.9°F–140.4°F)
- air inlet temperatures $T_{a,in}$: 20.2–25.2°C (68.4°F–77.4°F)
- air outlet temperatures $T_{a,out}$: 21.7–45.7°C (71.1°F–114.3°F)
- water flow rate F_w : 0.0091–0.284 L/s (0.144–4.51 gpm)
- air flow rate F_a : 0.22–0.76 m^3/s (428.4–1510.2 cfm)

For each test, the air-side inlet temperature was dependent on the room temperature. The temperature of the hot water was varied between 42.0°C (107.6°F) and 66.0°C (150.8°F) and could be controlled to within 1°C (1.8°F). For a fixed air flow rate, the water flow rate was changed so that the test can cover the laminar flow region, transitional region and fully developed turbulent

⁹Hewlett Packard, HP 3421A data acquisition system

flow region for water-side flow. Also for a fixed water flow rate, the coil heat transfer performance was studied with the change of air flow rate in a wide range. For this test program, the air-side flow rate changes in a range of 428 cfm \sim 1510 cfm. The variable range for water-side flow rate and inlet temperature are arranged as shown in Table 2.1.

Table 2.1: Ranges of Experimental Parameters

$T_{w,in}$ ($^{\circ}\text{C}$)	F_w (gpm)	V_a (m/s)
43.3	0.16–4.50	0.78, 1.31, 1.90, 2.74
54.4	0.14–4.50	0.78, 1.03, 1.31, 1.61 1.90, 2.19, 2.46, 2.74
65.6	0.16–4.50	0.78, 1.31, 1.90, 2.74

where V_a is the air-side velocity based on coil frontal area A_{fr} (equal to 18in \times 24in for the coil used in this experiment) given by

$$V_a = \frac{F_a}{A_{fr}} \quad (2.1)$$

For higher flow rate, the water flow rate going into the heat exchanger was measured by the flow meter calibrated over a range of 0.032–0.284 L/s (0.5–4.5 gpm). For very low flow rate in a range of 0.0091–0.032 L/s (0.144–0.5 gpm), the water flow rate was measured by draining water from the outlet of the heat exchanger into a graduated cylinder and measuring the water volume in a certain time period.

2.5 Calibration

2.5.1 Calibration of thermocouples

The thermocouples used for the experiment were all calibrated before they were used for the test. The calibration process is described in Figure 2.6. All thermocouples to be calibrated were immersed in a constant temperature bath. The temperature in this constant temperature bath can be set to be any value between -30°C and 100°C . The temperature in the bath was measured by using a calibrated standard thermometer. All of the thermocouples were connected into a connection box. This box was well isolated so that the temperature in the box was uniform. The temperature in this box, T_0 was measured using a thermocouple. The reference temperature was kept at 0°C by using a ice-point reference cell¹⁰. The output from the thermocouple system was measured by using the data acquisition unit and a Macintosh computer. During the test, the same system was used for data acquisition and data reduction. For the temperature range to be measured for this experiment, the thermocouples were calibrated for the temperature range of 10°C – 75°C . During the calibration process, the temperature in the constant temperature bath can be set. At steady state, taking the reading of the thermometer in the bath and recording the voltage output from the thermocouples.

As an example, the calibration curve for the thermocouple 1, which was used to measure the water-side inlet temperature, is shown in Figure 2.7. It has been found that the maximum measuring error (combination of calibrated error and

¹⁰TRC III, OMEGA Engineering, Inc.

precision error) for each thermocouple was less than 0.1°C (0.18°F).

2.5.2 Calibration of flow meter

The schematic for the calibration of flow meter is shown in Figure 2.8. A pre-calibrated rotameter was used for measuring the water flow rate passing through the flow meter. The water flow rate can be adjusted by setting the value. The calibration results are shown in Figure 2.9.

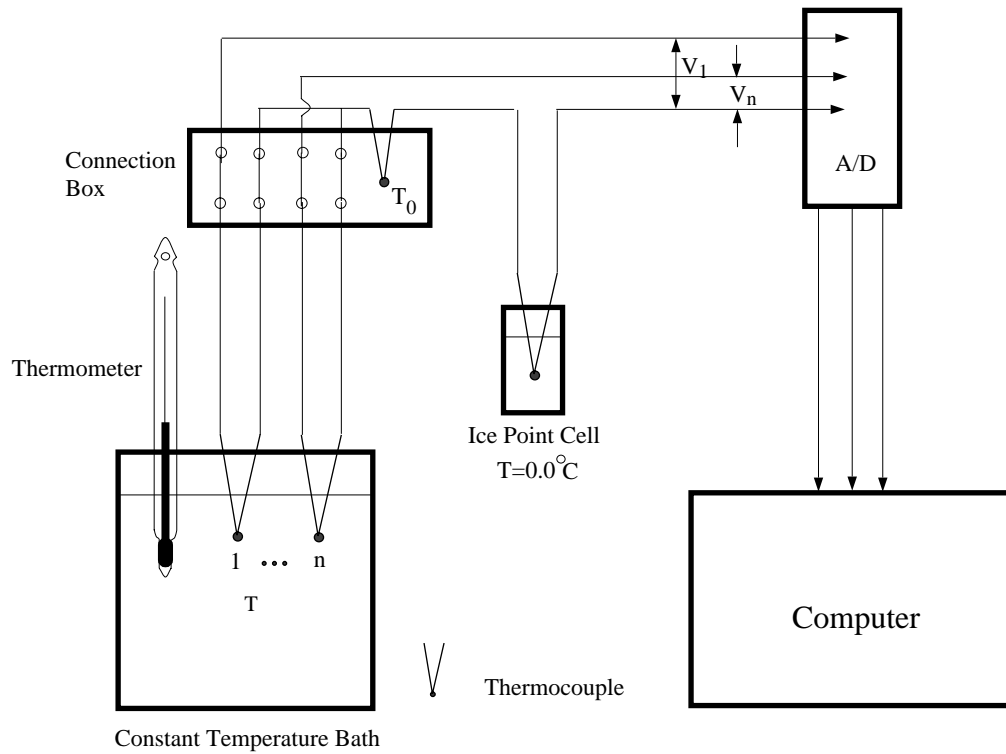


Figure 2.6: Schematic of thermocouple calibration

2.5.3 Calibration of wind tunnel

The calibration of the wind tunnel was performed with the coil mounted in the wind tunnel, using a Pitot-static tube mounted on a traverse, taking mea-

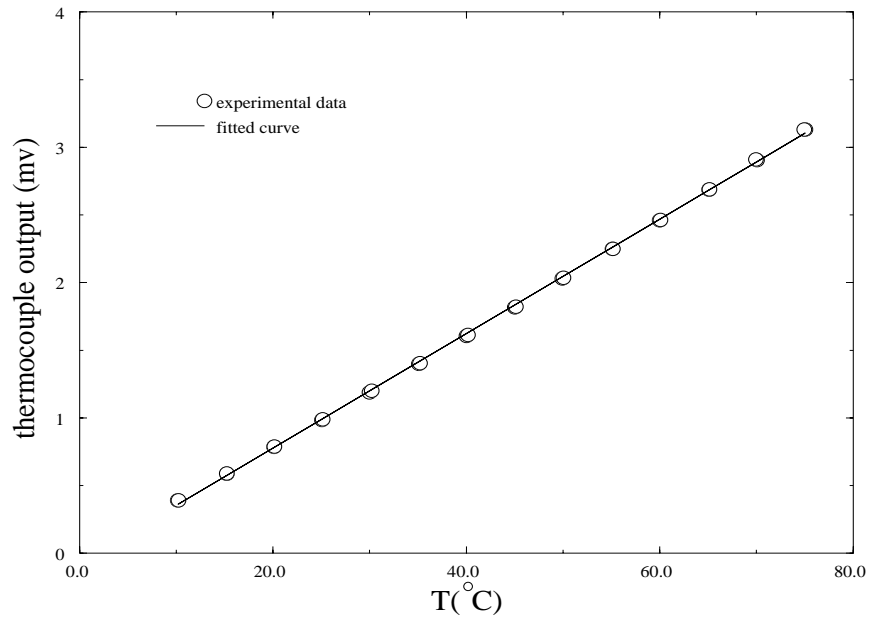


Figure 2.7: Calibration result for thermocouple 1

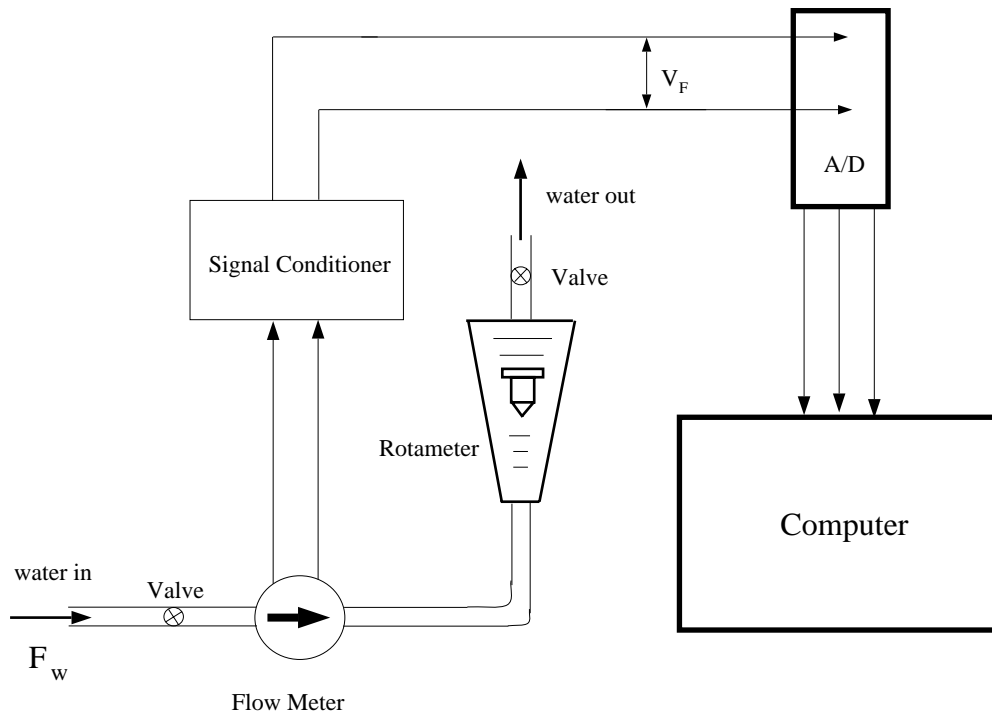


Figure 2.8: Schematic for calibration of flow meter

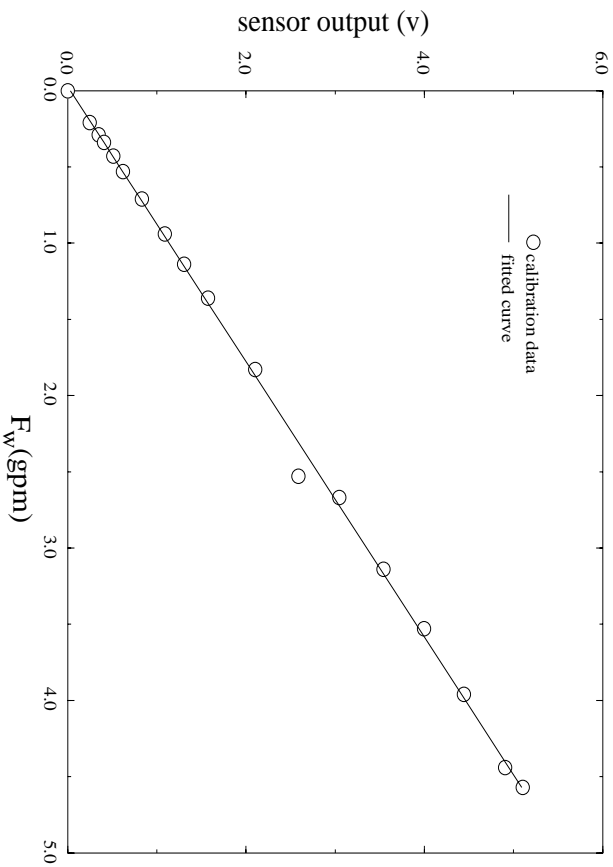


Figure 2.9: Flow meter calibration result

surements at discrete locations in the tunnel to measure velocity distribution across the tunnel section area, and then numerically integrating the velocities over the wind tunnel section area to obtain the total air flow rate for a given blower speed. The Pitot tube was connected to the differential pressure transducer. The air flow rate was determined by integrating the velocity over the wind tunnel section area. The velocity distribution along the horizontal centerline and vertical centerline in the tunnel are shown in Figure 2.10, where f_d is the blower driving frequency.

Because the air speed is determined uniquely by the blower's driving frequency, they can be correlated as shown in Figure 2.11.

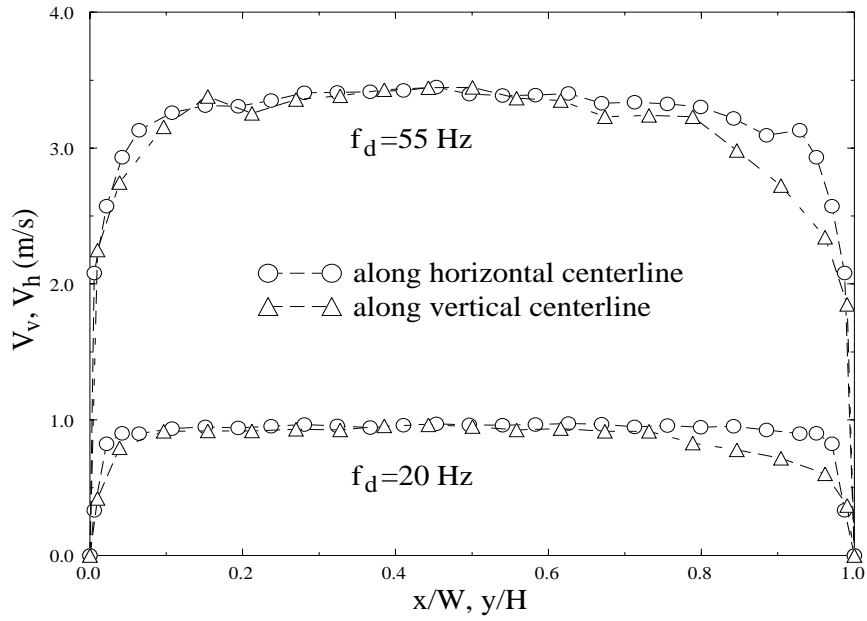


Figure 2.10: Velocity distribution along the horizontal and vertical centerlines of the wind tunnel

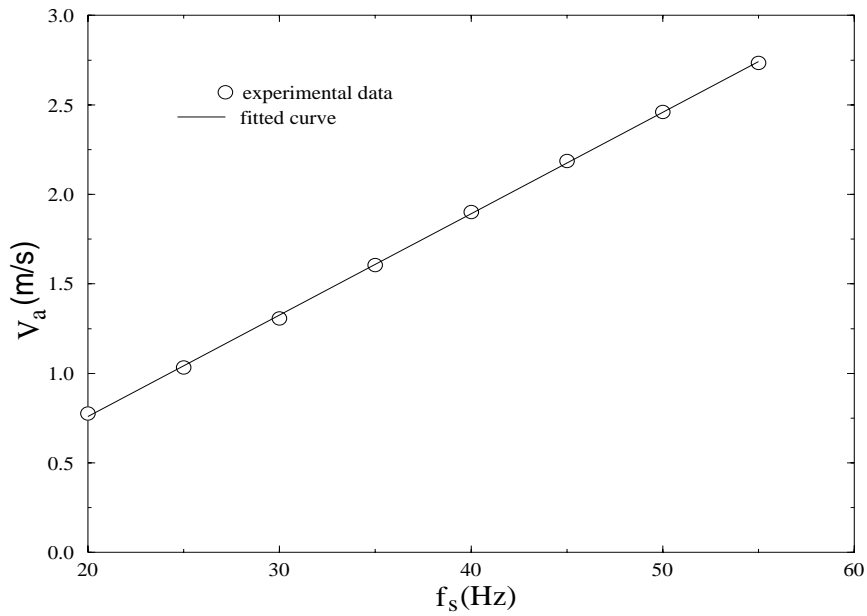


Figure 2.11: Wind tunnel calibration result

2.6 Temperature Measurement

Calibrated T-type thermocouples with error less than 0.1°C (0.18°F) were used to measure the temperatures. It was extremely important to ensure that the temperatures used in the calculations were the bulk temperatures.

2.6.1 Air-side temperature measurement

The air-side inlet temperature was close to the room temperature, which had uniform distribution. We applied only one thermocouple mounted in the upstream of the wind tunnel to measure the air-side inlet temperature. While at the outlet of the air-side, the air temperature distribution was not uniform. In order to measure the outlet bulk temperature of the air-side, we used five thermocouples, which were located near the entrance of the blower (see Figure 2.1) to measure the air-side outlet temperature. During test, the differences between the temperatures measured by these five thermocouples were not large, so the average value of these five temperatures was used as the mean bulk outlet temperature for the air-side of the heat exchanger.

2.6.2 Water-side temperature measurement

The water-side inlet and outlet temperatures were measured by single thermocouples. To make sure that these temperatures were close to the bulk temperature, both these measurements were made downstream of well-insulated 90° bends shown in Figure 2.12.

Mixing at the bends was expected to uniformize the temperature distribution so that a centerline measurement should be close to the bulk temperature.

Considerable effort was put in to estimate and minimize the error incurred by assuming the centerline and bulk temperatures to be the same. First, water temperatures were measured along the centerline moving away from the bend in the axial direction. Wall temperatures at the locations shown in Figure 2.12 for low and high water flow rates were also measured. These are shown in Tables 2.2 and 2.3. The coldest point on the wall was next to the metal casing of the heat exchanger due to conduction. At the inlet section, the existence of the lowest value is also due to conduction along the tube wall in the flow direction. Just after the outlet section, the water temperature is not uniform. The maximum non-uniformity for the temperature distribution along the tube inner cross section was measured by locating temperature probes in the same cross section plane as the thermocouples for measuring tube wall temperatures. This non-uniformity can be found by examining the temperature values listed in Tables 2.2 and 2.3, from which one can see that the true bulk temperature must be between the temperature measured by the probes and that measured by the tube wall thermocouples.

Table 2.2: Temperature ($^{\circ}\text{C}$) at inlet region

Water-side flow rate (L/s)	T_1	T_2	T_3	T_4	T_5
0.025	54.35	36.33	52.80	53.98	54.05
0.19	54.56	35.00	53.76	54.23	54.32

Using the water-side centerline temperature as the bulk temperature will lead to some error in the final results. The wall and centerline temperatures

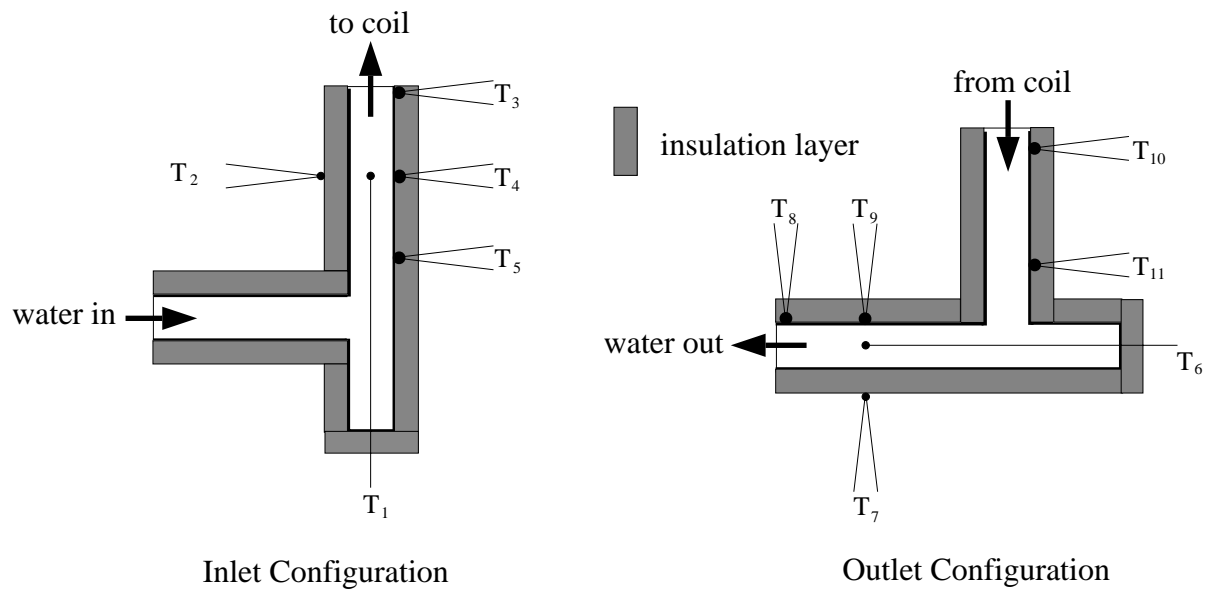


Figure 2.12: Inlet and outlet sections

Table 2.3: Temperature ($^{\circ}\text{C}$) at outlet region

Water-side flow rate (L/s)	T_6	T_7	T_8	T_9	T_{10}	T_{11}
0.025	35.42	28.83	35.21	35.34	34.21	35.09
0.19	47.72	34.21	47.32	47.52	46.98	47.37

discussed above provide a range of values within which the bulk temperature should lie. These temperature bounds were used in the data reduction procedure to be discussed later to estimate the uncertainty in the output values: it is less than 5% in the overall heat transfer coefficient, and less than 5% in the air-side heat transfer coefficient. For the water-side heat transfer coefficient, the uncertainty changes significantly with flow rates. For low flow rates, it is always less than 2% but becomes 12% at the highest water flow rate. The upper value is highly conservative since at high flow rates the centerline temperature can actually be expected to be closer to the bulk temperature. Also at higher water flow rates, the water-side thermal resistance is much smaller than the air-side thermal resistance, so that the uncertainty in the overall heat transfer coefficient is always low.

CHAPTER 3

DATA ANALYSIS BY LEAST-SQUARES METHOD

3.1 Introduction

The overall thermal resistance, $R(= 1/UA_a)$, between the water and air is the sum of the water-side thermal resistance, $R_w(= 1/h_wA_w)$, and the air-side thermal resistance, $R_a(= 1/\eta h_a A_a)$, where we have neglected the tube wall thermal resistance. R can be determined from measurements, but splitting it into its components R_w and R_a is not easy. One common way is to assume the heat transfer correlation on the water-side so that the air-side correlation can be determined. The difficulty here is that no water-side correlation which includes the effect of coil bends is available. The common practice is to use those based on straight pipes.

3.2 Background on Data Analysis

3.2.1 Extrapolation method

This method was suggested by Wilson (1915). If the air-side flow rate is held fixed, R_a is constant. The water-side flow rate can then be varied to find R as a function of R_w . Extrapolating the result to $R_w \rightarrow 0$, which corresponds to an infinite flow rate, we get $R \rightarrow R_a$. In a similar fashion R_w can be kept constant, and R_a varied and the $R_a \rightarrow 0$ limit will give $R \rightarrow R_w$. An important study using this technique was reported by Shepherd (1956) who worked with several different heat exchangers. The method has the advantage in that the air-side heat transfer coefficient can be obtained from experimental data without using an assumed heat transfer correlation for the water-side. However, it cannot give the non-dimensional heat transfer coefficients. This is because the tube wall temperatures cannot be determined when extrapolating either R_w or R_a to zero. Another disadvantage of this method is that the results are obtained by extrapolating from actual data to infinite flow rates. Physical phenomena that come into play at flow rates higher than those actually used in the experiments are not taken into account.

3.2.2 Log-mean temperature difference method

In the heat exchanger literature, it is a general practice that an overall heat transfer coefficient, U , is utilized on the basis of the use of a log-mean temperature difference of the two fluids, regardless of the flow configurations of the two fluids. This practice is applied even in the case of of single-row coil (Shepherd, 1956) for which the log-mean temperature difference has no

practical meaning, since all tubes in the coil are exposed to the same inlet air. Consequently, this method must be discarded in dealing with single-row coils.

3.3 Least-Squares Power-Law Method

Because of the difficulties discussed above we propose a different data analysis procedure. We introduce an overall heat transfer coefficient, U , defined so that the local heat transfer from the water to the air is given by $UA_a(T_w - T_{a,in})$. Then we can derive the equation for U based on cross flow model shown in Figure 3.1.

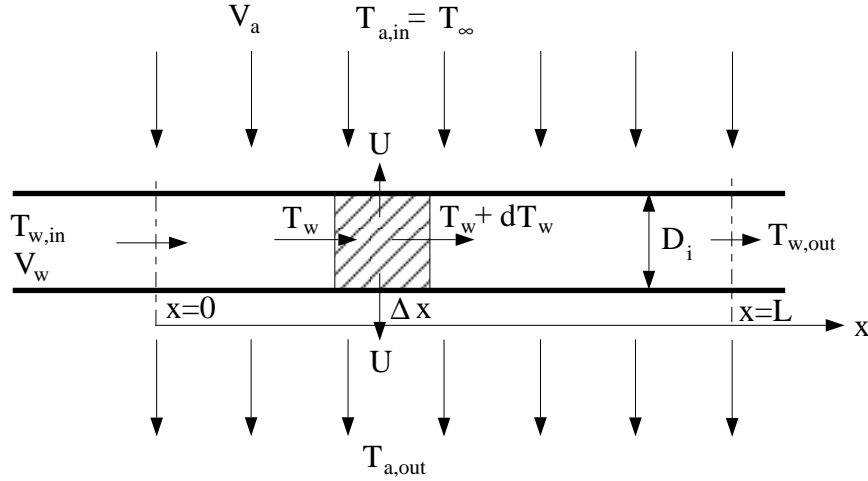


Figure 3.1: Schematic model of cross-flow heat exchanger

Assuming U to be constant over the heat exchanger tube length and applying energy balance to the water-side, we have

$$U(T_w - T_{a,in})pdx = \rho_w c_{pw} (V_w \pi D_i^2 / 4) (-dT_w) \quad (3.1)$$

or

$$-U p dx = \rho_w c_{pw} (V_w \frac{\pi D_i^2}{4}) \frac{dT_w}{T_w - T_{a,in}} \quad (3.2)$$

Integrating equation (3.2) from $x = 0$ to $x = L$ and applying boundary conditions for T_w , we can get the following expression for U :

$$U = \frac{\rho_w(\pi D_i^2/4)V_w c_{pw}}{A_a} \ln \frac{T_{w,in} - T_{a,in}}{T_{w,out} - T_{a,in}}. \quad (3.3)$$

The total heat transfer rate of the heat exchanger, Q , can be given by

$$Q = \rho_w V_w c_{pw} (T_{w,in} - T_{w,out}) \quad (3.4)$$

$$= \rho_a V_a c_{pa} (T_{a,out} - T_{a,in}). \quad (3.5)$$

The total thermal resistance is

$$\frac{1}{UA_a} = \frac{1}{\eta h_a A_a} + \frac{1}{h_w A_w} \quad (3.6)$$

where we have neglected the thermal resistance of the tube wall. η is the total efficiency of the air-side surface given by

$$\eta = \frac{\eta_0 A_f + A_t}{A_a} \quad (3.7)$$

where the fin efficiency η_0 is a function of h_a . Since η and h_a appear together in equation (3.6), we will determine the product ηh_a . The present experiments do not enable η to be experimentally determined. More importantly, it is the product ηh_a that is needed to find the air-side thermal resistance and in turn the heat transfer, which is ultimately what the designer is interested in.

The air- and water-side correlations between the Nusselt numbers and the flow Reynolds numbers are commonly expressed in power-law forms. So it is reasonable to assume that

$$\eta Nu_a = a_1 Re_a^m Pr_a^{1/3} \quad (3.8)$$

$$Nu_w = b_1 Re_w^n Pr_w^{0.3} \quad (3.9)$$

The water- and air-side Reynolds numbers are defined as $Re_w = D_i V_w / \nu_w$ and $Re_a = V_a \delta / \nu_a$, respectively. V_w is the water-side velocity, and V_a is the air-side face velocity based on the frontal area of the heat exchanger. It should be pointed out here that Re_a has been defined in the literature in other ways, e.g. with the length scale being a hydraulic diameter (Kays and London, 1984), or equal to the tube outer diameter plus two times the collar thickness (Kayansayan, 1993). The definition used here is similar to that of Mirth, et al., 1993. The Prandtl number exponent for the water-side correlation is taken from the Dittus-Boelter equation, while the air-side Prandtl number exponent is from the Colburn analogy (Colburn, 1933).

Using equation (3.6), we obtain

$$\frac{1}{UA_a} = \frac{\delta}{A_a k_a a_1 Pr_a^{1/3}} Re_a^{-m} + \frac{D_i}{A_w k_w b_1 Pr_w^{0.3}} Re_w^{-n} \quad (3.10)$$

The properties of water are evaluated at the average of its inlet and outlet temperatures $(T_{w,in} + T_{w,out})/2$. The properties of air are at the film temperature $[T_{w,m} + (T_{a,in} + T_{a,out})/2]/2$.

The data reduction procedure is as follows. From the raw experimental data, the overall heat transfer coefficient U is first determined from equation (3.3) for each test run. The four constants a_1 , b_1 , m and n are then found from all test data and equation (3.10) by a least-squares procedure that minimizes the deviation from $1/UA_a$ in equation (3.10). The detailed procedures of this approach and its Fortran code can be found in Appendix-B and Appendix-C, respectively.

3.4 Results and Discussion

The water- and air-side velocities were varied in the 0.036–1.64 m/s and 0.78–2.74 m/s range, respectively. Heat balance tests showed that the maximum difference between the heat given up by the water and the heat acquired by the air as computed from the measurements was less than 5% for most of the data used in this paper. For very low water flow rates, around 0.0091–0.032 L/s (0.144–0.5 gpm), this difference increased but was less than 10%. The average values of the water-side and air-side heat transfer rates were used for the calculations of total heat transfer rates of the heat exchanger.

An uncertainty analysis has been carried out on the experimental data. Uncertainty in heat transfer comes from the propagation of bias errors, in which the sensor's calibration error, data acquisition error and data reduction error have been considered, and precision errors which come from the scatter in data due to multiple measurements. The uncertainty was calculated following the method described by Kline and McClintock (1953) with 95% confidence level. The analysis demonstrates that the maximum uncertainty is 10–18% for the data at very low water flow, and less than 8% for the rest. The detailed procedure for the uncertainty analysis can be found in Appendix-A.

A total of 259 sets of data were chosen for presenting the current results with combinations of different air velocity, water velocity, and inlet water temperature. From a least-squares power-law analysis of the data, the air- and water-side heat transfer correlations were obtained.

3.4.1 Air-side heat transfer

The heat transfer correlation for the air side is

$$\eta Nu_a = 0.074 Re_a^{0.59} Pr_a^{1/3} \quad \text{for } 180 < Re_a < 700 \quad (3.11)$$

From this the air-side efficiency-heat transfer coefficient product ηh_a can be calculated.

Comparing the present air-side heat transfer correlation with those in the literature is difficult. The reason is that we have applied a cross-flow mathematical model, equation (3.3), to calculate the overall heat transfer coefficient. The commonly used method for calculating overall heat transfer coefficient is based on the counter-flow log-mean temperature difference to which a correction factor is applied. This correction factor is not known, though the value of unity has been suggested for multiple row heat exchangers (Stevens, et al., 1957). For a single-row heat exchanger it is not clear that the value of unity should apply. As a rough comparison, however, the exponent of Re in the present air-side heat transfer correlation (3.11) is 0.59, which can be compared with the value of 0.51 calculated from the correlation of Gray and Webb (1986) for a single-row heat exchanger with plate fins. In principle quantitative comparison can be made in either of the following ways: data from other sources can be processed using our method, or, based on the present least-squares procedure, our data can be processed using the incorrect log mean temperature method. Due to absence of detailed experimental data from other sources, we are left only with the latter option. Comparison of our data processed in this fashion with the correlation of McQuiston (1981) is shown in Figure 3.2. The differences are small.

We can also process our experimental data using the extrapolation method.

This is shown in Figure 3.3. There is reasonably good agreement between the two methods though the extrapolation method always gives lower air-side heat transfer coefficients than the least-squares power-law method. Nevertheless, the disadvantages of the extrapolation method of Wilson discussed previously still stand.

3.4.2 Water-side heat transfer

The correlation for the water side obtained from experimental data is

$$Nu_w = 0.03 Re_w^{0.79} Pr_w^{0.3} \text{ for } 1200 < Re_w < 5.3 \times 10^4 \quad (3.12)$$

This correlation can be compared with predictions based on published heat transfer correlations in a straight pipe. For a specific test run we know the air and water flow rates, from which Re_a and Re_w can be determined. Standard correlations then provide the heat transfer coefficient. The total heat transfer rate is given by equations (3.4) and (3.5).

The following correlations are commonly used for in-tube heat transfer calculations:

(a) *Dittus-Boelter (1930)*:

$$Nu_w = 0.023 Re_w^{0.8} Pr_w^{0.3} \text{ for } Re_w > 10^4 \quad (3.13)$$

(b) *Sieder-Tate (1936)*:

$$Nu_w = 1.86 Re_w^{0.33} Pr_w^{0.33} \left(\frac{D_i}{l}\right)^{0.33} \left(\frac{\mu_b}{\mu_s}\right)^{0.14} \text{ for laminar flow} \quad (3.14)$$

where μ_b/μ_s is the ratio of the fluid viscosity at fluid bulk temperature and at tube wall temperature.

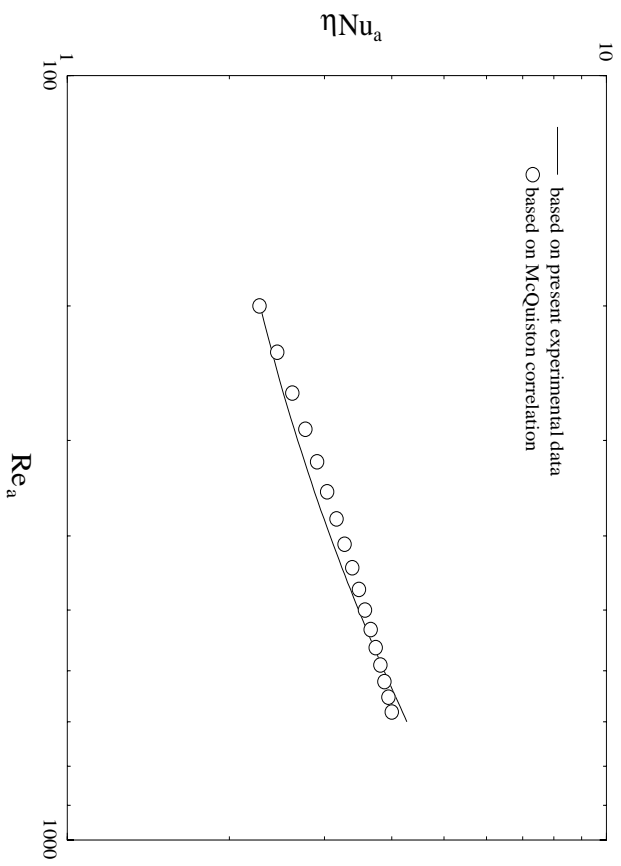


Figure 3.2: Air-side Nusselt number

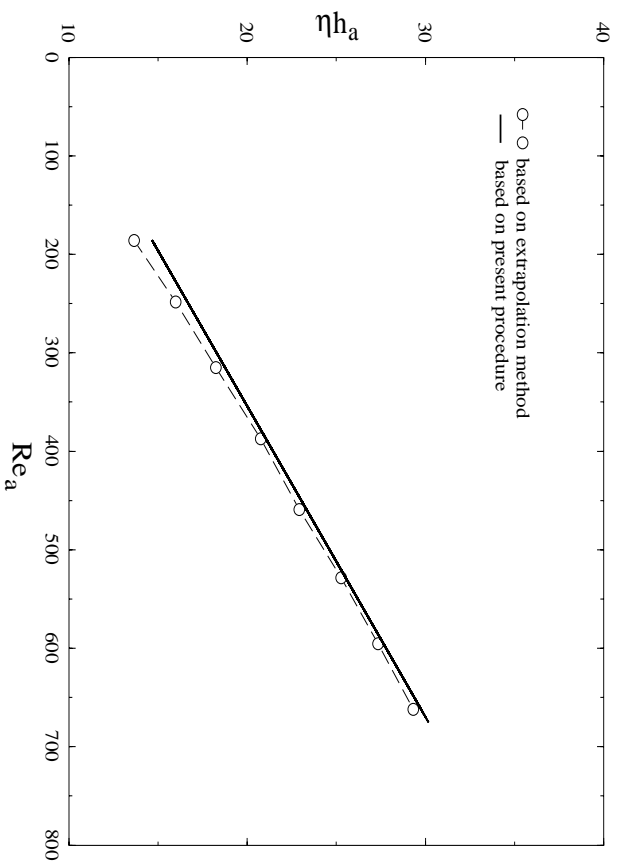


Figure 3.3: Air-side heat transfer coefficients, compared to extrapolation method result

(c) *Gnielinski (1976)*:

$$Nu_w = \frac{(f_w/8)(Re_w - 1000)Pr_w}{1 + 12.7(f_w/8)^{1/2}(Pr_w^{2/3} - 1)} \text{ for } 2,300 < Re_w < 5 \times 10^6 \quad (3.15)$$

where

$$f_w = (0.79 \ln Re_w - 1.64)^{-2} \quad (3.16)$$

(d) *Petukhov (1970)*:

$$Nu_w = \frac{(f_w/8)Re_w Pr_w}{1.07 + 12.7(f_w/8)^{1/2}(Pr_w^{2/3} - 1)} \left(\frac{\mu_b}{\mu_s} \right)^{0.25} \text{ for } 10^4 < Re_w < 5 \times 10^6 \quad (3.17)$$

where f_w is again from equation (3.16).

In heat exchanger work, the Dittus-Boelter correlation, equation (3.13), is recommended by the industry standard (ARI, 1987) for the calculation of water-side heat transfer for $Re_w > 3100$. Whether it can be used to predict accurate heat transfer coefficients for flow in a heat exchanger tube has been questioned by some research workers (Mirth, et al., 1993).

Comparison between our result, equation (3.12), and the above correlations is shown in Figure 3.4. The Dittus-Boelter (3.13), Gnielinski (3.15), Sieder-Tate (3.14) and Petukhov (3.17) correlations are shown. The Nu_w values are plotted for a wide range of Re_w , sometimes outside the recommended range of validity of the correlation. The Dittus-Boelter correlation is lower than the other turbulent flow correlations. We also notice that for high Reynolds numbers, which corresponds to fully developed turbulent flow, the Nusselt numbers that we have obtained are not much different from the others since in a highly turbulent flow the effect of the bends is relatively unimportant. Our proposed correlation is closest to the Gnielinski and Petukhov predictions for $Re_w > 10,000$. It is some-

times claimed (Mirth, et al., 1993) that the Gnielinski equation (3.15) is valid for $Re_w > 2,300$. However, this is not supported by the present data. At low Re_w also, down to $Re_w=1200$, the Petukhov correlation is reasonably close even though it was designed for higher values of Re_w . This is due to the transverse mixing effect of the secondary flow at the bends which leads to a turbulent-like heat convection. For this reason the Sieder-Tate correlation, which is usually used for heat transfer calculation in a straight pipe in the laminar regime, consistently predicts a much lower heat transfer rate in the laminar as well as in the turbulent regime.

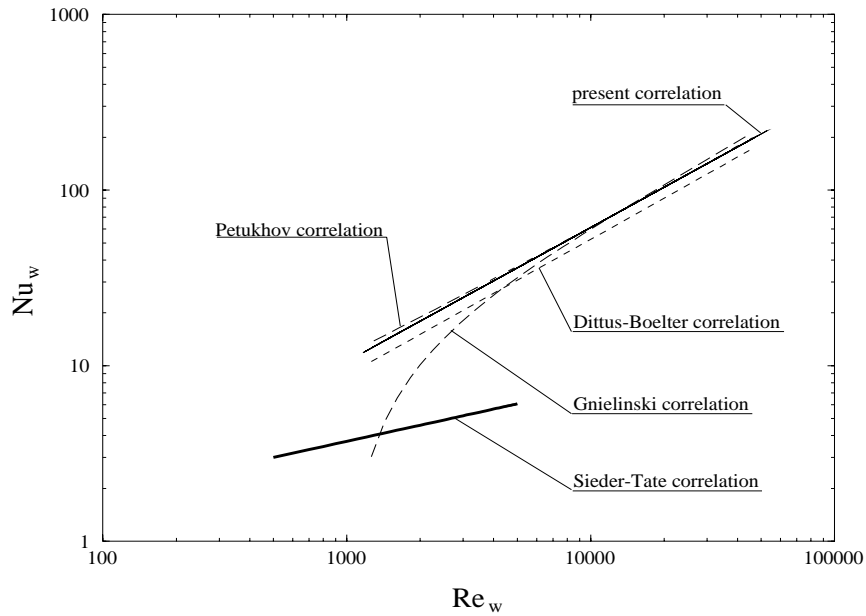


Figure 3.4: Water-side heat transfer correlation, compared to straight tube correlations

3.4.3 Effect of bends on water-side heat transfer

Centrifugal forces in a tube bend lead to a secondary flow consisting of a pair of symmetric counter-rotating vortices in a cross section normal to the main flow direction. The secondary flow can significantly enhance heat transfer in the bend region. Though in our experiments the bends were insulated, the secondary motion persists well into the straight section following the bend. Extensive literature exists for the related problem of helically coiled tubes (see the review by Shah and Joshi, 1987). There is also some work on flow and heat transfer in a straight tube following a bend. Cheng and Yuen (1987) applied flow visualization techniques to observe the evolution of secondary flow and its decay in a straight pipe downstream from a 180° bend. Heat transfer experiments have been done by many researchers. Ede (1966) measured the temperature distribution in a straight tube downstream from a 180 degree bend, but did not calculate local heat transfer coefficients. Lis and Thelwell (1963-1964), Tailby and Staddon (1970) and Moshfeghian and Bell (1979) provided local heat transfer correlations for turbulent flow.

In the turbulent region, all of the experimental data that are in the above papers are correlated for local heat transfer, while our heat transfer correlation is for the average value. Also for our case, the water was being cooled inside the bend tube. The only similar results are those of Tailby and Staddon (1970), which were developed for a fluid being cooled. For purposes of comparison, we integrated this local heat transfer correlation from the end of one bend to the

start of the next, to get the following average Nusselt number correlation

$$Nu_w = 0.0987 \left(\frac{D_i}{L_s}\right) Re_w^{0.82} Pr_w^{0.4} \left(\frac{R_c}{D_i}\right)^{0.85} \left[1 + \frac{L_s}{\pi R_c}\right]^{0.96} - 1 \quad (3.18)$$

Another turbulent flow local heat transfer correlation is that of Moshfeghian and Bell (1979), which was developed for the case of fluid being heated. The following average heat transfer correlation can be obtained

$$Nu_w = 0.0931 \left(\frac{D_i}{L_s}\right) Re_w^{0.825} Pr_w^{0.4} \left(\frac{\mu_b}{\mu_s}\right)^{0.14} \left(\frac{R_c}{D_i}\right)^{0.884} \left[1 + \frac{L_s}{\pi R_c}\right]^{0.884} - 1 \quad (3.19)$$

Laminar flow correlations have been provided only by Moshfeghian and Bell (1979). Unfortunately, their correlation, as written, is not consistent with the experimental data they show, and hence will not be used here. For purposes of comparison we have shown in Figure 3.5 the Nusselt number in a helical coil. A widely used laminar flow correlation is that of Kalb and Seader (1974) given by

$$Nu_w = 0.836 De^{0.5} Pr_w^{0.1} \text{ for } Re(D_i/2R_c)^{1/2} > 80, 0.7 < Pr_w < 5.0 \quad (3.20)$$

This is merely an upper bound if we remember that in the straight part of the heat exchanger where heat transfer actually occurs, the secondary motion is decaying.

The results of the comparison are shown in Figure 3.5. It can be seen from this figure that the heat transfer coefficient of the flow in bends is always larger than flow in a straight tube downstream from a U-bend, due to the decay of secondary flow in straight tube. For turbulent and transitional flow, the Moshfeghian and Bell correlation (equation 3.19) gives higher heat transfer coefficients than the current correlation, while equation (3.18) gives much higher (about 20%) heat transfer values.

3.4.4 Overall heat transfer

The quality of the least-squares power-law correlation with respect to measured data can be judged from Figure 3.6 which shows $(UA_a)^{-1}$ computed both from equations (3.11) and (3.12), and from experiments. The maximum variation between measurements and correlations is 10%.

Figures 3.7 and 3.8 show Q as a function of Re_w for two different air flow rates. The predicted values are obtained from correlations (3.11) and (3.12) by using a discretization method similar to that of Mirth, et al. (1993). Data from actual measurements are also shown along with the values computed from the manufacturer's catalog which are only for $Re_w > 5,000$. There is good agreement between the three sets of values. Similar results are obtained for other air flow rates. The experiments were carried out for a wide range of water-side Reynolds numbers, including both turbulent and laminar regimes, but only the data for $Re_w < 20,000$ are shown in the figures. The smoothness of the Q - Re_w curve without jump or hysteresis at transition is significantly different from that in a straight pipe. The bends appear to introduce enough secondary flow for the nature of laminar to turbulent transition to be qualitatively affected.

3.5 Conclusions

A single-row heat exchanger was tested with hot water in the in-tube side and air flow over. By assuming power-law forms of the Nusselt-Reynolds number relation, best-fit correlations for both air- and water-sides could be obtained. Based on our definition for U (equation (3.3)), the Nusselt number-Reynolds number correlations that resulted from this procedure are represented by equa-

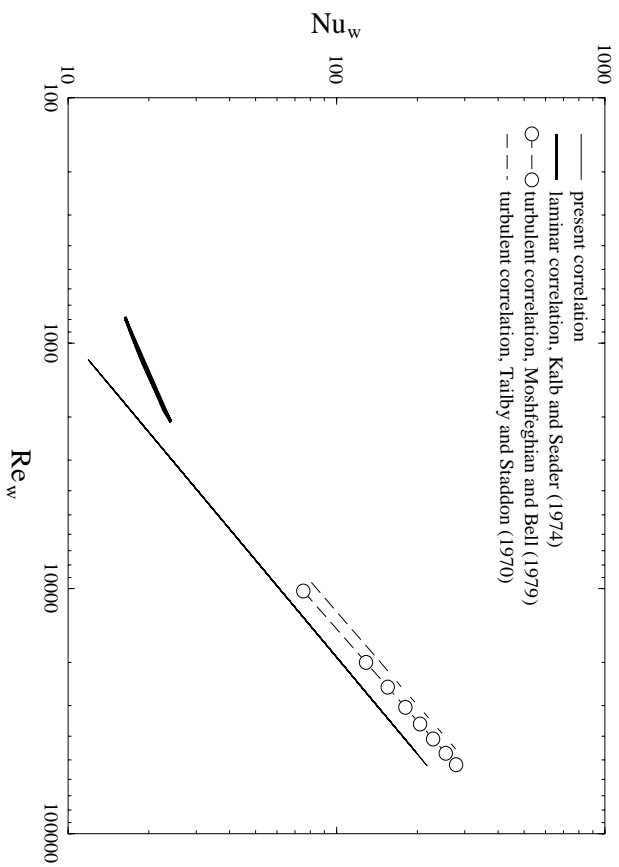


Figure 3.5: Effect of bends on water-side Nusselt number

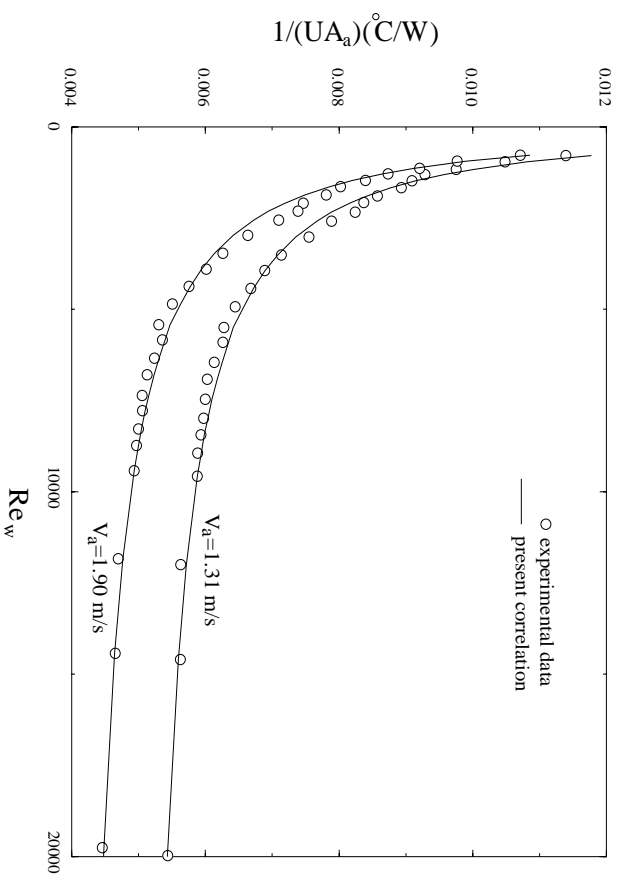


Figure 3.6: Comparison of experimental data with power-law least-square results

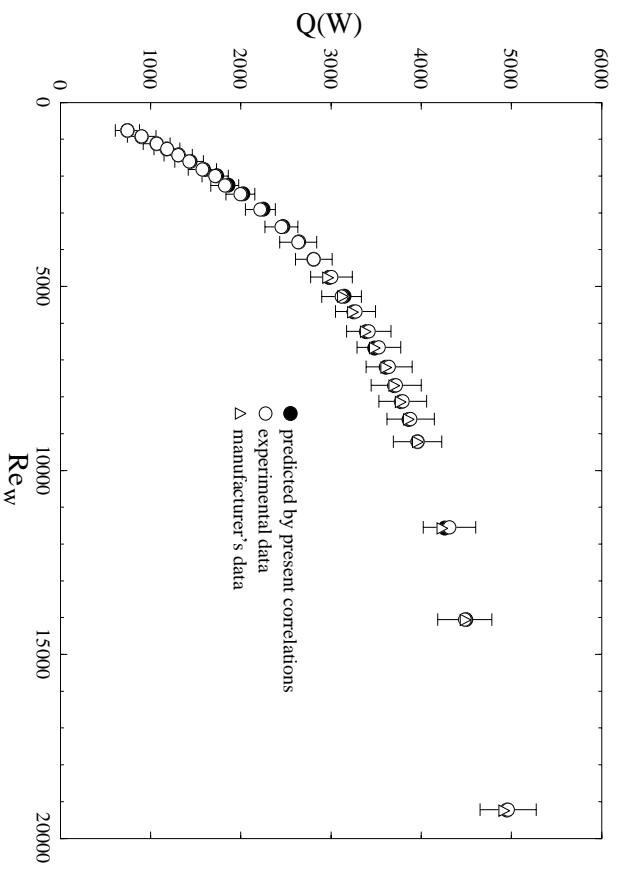


Figure 3.7: Heat transfer rate for $V_a = 1.31$ m/s, $T_{w,in} \approx 54.0^\circ\text{C}$, $T_{a,in} \approx 21.0^\circ\text{C}$

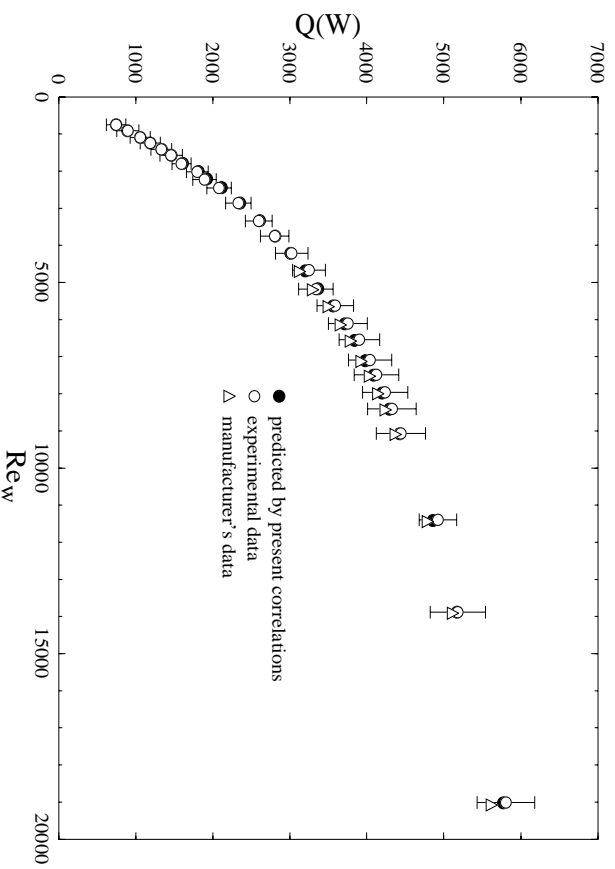


Figure 3.8: Heat transfer rate for $V_a = 1.90$ m/s, $T_{w,in} \approx 54.0^\circ\text{C}$, $T_{a,in} \approx 21.0^\circ\text{C}$

tions (3.11) and (3.12). The water-side correlation is closest to the correlation of Petukhov (3.17). The results also show the strong influence of the heat exchanger bends in laminar and transition heat transfer. Straight-pipe laminar flow heat transfer correlations are found to be inapplicable due to the presence of secondary flows.

CHAPTER 4

DATA ANALYSIS BY NEURAL NETWORK METHOD

4.1 Introduction

Artificial neural networks have been developed in recent years and used in many application areas. Its most attractive advantage is that it allows modeling of a non-linear complex system without requiring knowledge of any explicit functional relationship that may exist between the input and output variables of the system. Theoretically it has been shown that a continuous neural network with two hidden layers can approximate any continuous function by using any fixed, continuous, sigmoidal non-linearity (Cybenko, 1989). The neural network technique has been successfully used in many research and industrial environments, such as in object/pattern recognition, image labeling, non-linear control, optimization, etc. (Lisboa, 1992). The importance of neural networks and their applications has been widely recognized. In 1988, ANNIE (Application of Neural Network for Industry in Europe) was established in Europe to investigate the performance of neural networks in industrial applications, and to compare

with conventional approaches. The work done by ANNIE can be found in its research report (Croall and Mason, 1991). The importance of neural networks has also been realized by many researchers in the area of mechanical engineering. It has been used to simulate a highly non-linear system or the chaotic dynamics of fluid flow such as the Lorenz system (Fan, et al., 1993, Welstead, 1992). The neural network technique has been used for the control of transition of flow from laminar to turbulent states (Fan, et al., 1993). For more complicated flows, neural networks have been successfully used for real-time prediction and control of 3-D unsteady separated flows (Faller, et al., 1994), and even for the control of turbulent flow and drag reduction (Jacob and Reynolds, 1993). In the chemical area, neural networks have been successfully used to model and control chemical systems with non-linear characteristics (Bhat, et al., 1992).

Experimental investigations are very important in heat transfer studies. In many of these, one expects to reduce experimental data into one or more compact equations or correlations. Based on theoretical analyses or semi-empirical knowledge, the forms of the equations are usually assumed and certain free constants are then determined from experimental data. A least-squares regression approach, or partial least-squares regression approach, (Geladi and Kowalski, 1986) can be used for the determination of these constants as in the previous chapter. We present here the neural network method as a viable alternative in which no relation between the quantities being correlated need be assumed. Thibault and Grandjean (1991) were the first to apply the method to a heat transfer problem. A simple thermocouple lookup table problem and two much more complicated problems with non-dimensional heat transfer coefficients were

presented for the correlation of heat transfer data using neural networks. In Lombardi, et al. (1994), the neural network method was applied to correlate experimental data for two-phase pressure drops in horizontal ducts.

The experimental study of heat exchangers falls within the category of heat transfer experiments described above. There is one fluid medium (e.g. water) flowing within the tube of the heat exchanger, and another one (e.g. air) passing over the fins of the heat exchanger. The heat transfer characteristics of the heat exchanger are commonly expressed through heat transfer correlations for either side. The main disadvantage of the correlation method is that the heat transfer correlations strongly depend on the definitions of heat transfer coefficient and the temperature difference. Also this method has a disadvantage for the application in that an iterative method is inevitable when applying the correlations to a specific design problem due to the coupling between the results (such as the fluid temperature) and the parameters used to obtain them (such as the fluid properties). All of these disadvantages can be overcome by using neural network method through inputting data directly into a trained neural network to get the desired output from the network without involving the definitions of heat transfer coefficient or appropriate temperature difference. This advantage of neural networks can be seen clearly in the following sections.

The objective of this chapter is to apply a neural network technique to model the heat transfer performance of a heat exchanger by training a neural network with experimentally obtained training data. The trained neural network will then be used to predict the behavior of the heat exchanger. Finally the predicted results will be compared with new experimental data. Comparison of

the performance of the neural network and least-squares power-law methods of Chapter 3 is also carried out.

4.2 Background on Neural Networks

A neural network, as its name implies, uses configurations like those found in the human brain to mimic the non-linear relation between its input and output. Figure 4.1 illustrates a typical network configuration. There are two types of elements in a neural network: *nodes* and their *connections*. The node, sometimes called a processing element or neuron, is the basic processor of a neural network. There is a real number associated with each connection, which is called the *weight* of the connection. Typically the nodes of a network are grouped together into clumps called *layers*. The network shown has three layers: an input layer, an output layer, and one hidden layer. Note that each node from the input layer is connected to all of the nodes of the hidden layer. The same is true between the hidden and output layers. Such a connection scheme is called a *fully connected* network scheme. Note that the nodes in the same layer are not connected to each other for the case shown in this figure.

A typical simulation of a node is illustrated in Figure 4.2. For each node, there is an *activation* associated with it. In this figure, the activation s_j of node j is determined by multiplying all inputs (including a bias), which are connected to this node, by weights and taking their sum as

$$s_j = \sum_{i=1}^n x_i w_{ij} \quad (4.1)$$

The output of the node is the result of a transfer function on the activation.

Usually, transfer functions are non-linear threshold functions, which are confined to the range (0,1). A commonly used threshold transfer function in neural network is a sigmoid function (This function and its derivative are shown in Figure 4.3).

$$y_j = f(s_j) = \frac{1}{1 + e^{-s_j}} \quad (4.2)$$

This highly nonlinear function determines the highly non-linear property of the neural network. There is a bias unit associated with the node, which determines the spontaneous activity of the node. The bias unit has a constant output of 1. The use of a bias unit for each node can improve the convergence property of a neural network during the training process (Dayhoff, 1990). For the nodes in the input layer, they do not perform the weighted sum on their inputs. Each node in the input layer takes the value directly from the input data.

By varying the weights of the different connections, an output can be made to follow a certain input relationship. In other words, the network can be trained to model a non-linear relation between multiple inputs and outputs. The changing of the weights is achieved through a supervised learning process. The input is propagated through the network and the calculated output is compared with the actual output, which is called the target output of the neural network. The error between the desired outputs and the target outputs are measured. Usually, a neural network uses a back propagation algorithm to adjust the weights of the connections. This process is done iteratively until the error is within a certain tolerance.

By comparing the outputs from the output layer of a neural network with the target output, the network adjusts connection weights in the following way

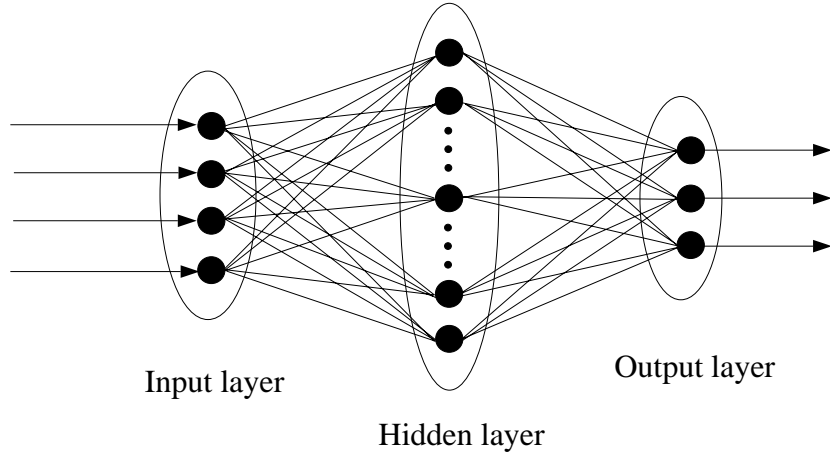


Figure 4.1: Configuration of a simple neural network

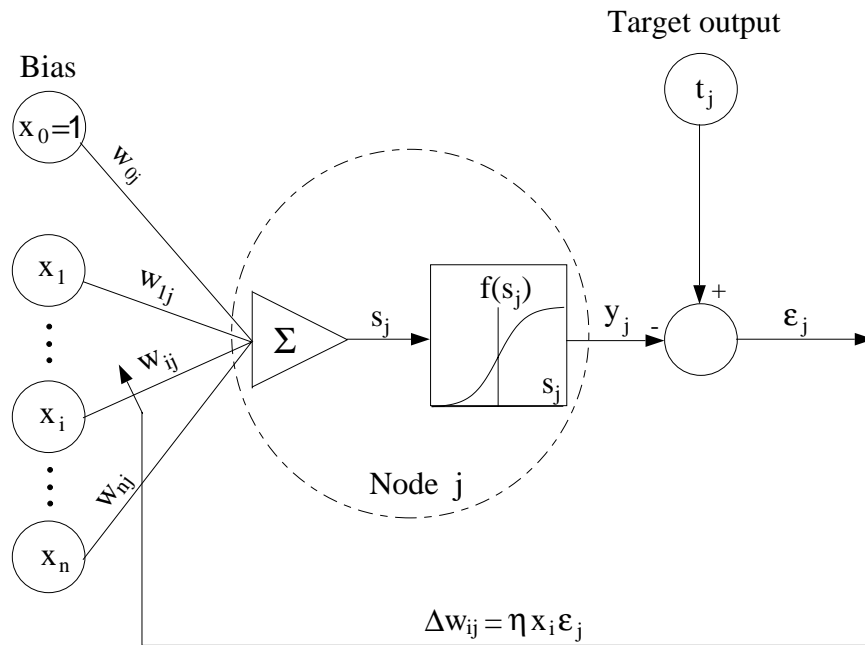


Figure 4.2: Typical model of a single node

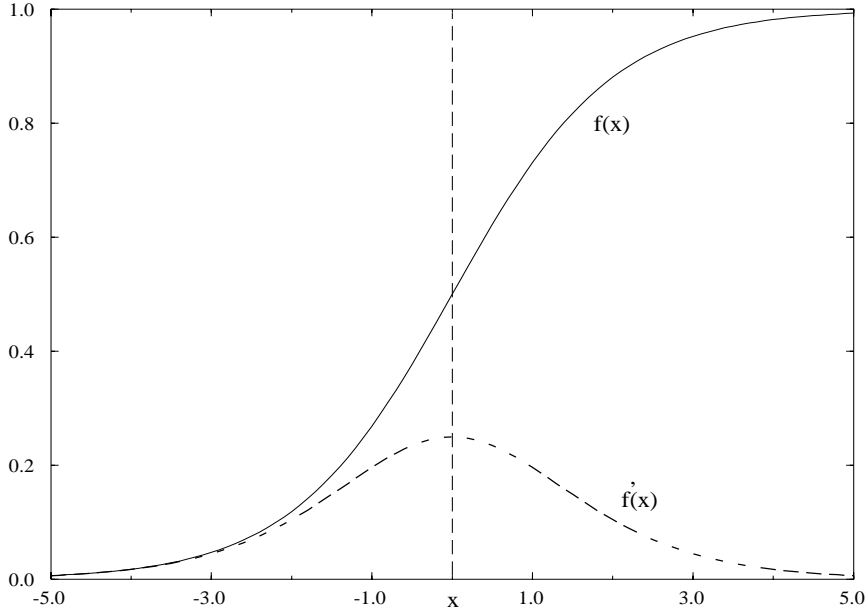


Figure 4.3: Sigmoid function and its derivative

(Dayhoff, 1990)

$$\Delta w_{ij} = \xi x_i \epsilon_j \quad (4.3)$$

where ξ is called the *training rate*, ϵ_j is the error value. For the output layer, ϵ_j can be determined as (Dayhoff, 1990)

$$\epsilon_j = (t_j - y_j) f'(s_j) \quad (4.4)$$

where $f'(s_j)$ is the derivative of the sigmoid function (as shown in Figure 4.3).

If node j is in a hidden layer, the error value is computed as (Dayhoff, 1990)

$$\epsilon_j = \left[\sum w_{jk} \epsilon_k \right] f'(s_j) \quad (4.5)$$

where the sum is taken of the ϵ values of all nodes that receive output from node j .

The drawbacks of the back propagation algorithm appear to be the long convergence time and the fact that it can easily get stuck to a local minimum. Improvement of convergence speed can be realized by varying the learning rate dynamically or by using “momentum” terms (Lippman, 1987). Different methods have been developed (Dayhoff, 1991) which include changing the network, rearranging training data, and adding random noise to the weights to allow a back propagation network to escape from a local minimum to a global minimum. For more details about the neural network and its application, one is referred to the the book by Nelson, et al. (1991).

4.3 Neural Network Method

The neural network configuration used for the analysis of the heat exchanger data is shown in Figure 4.4. There are three layers in this configuration, the left layer is the input one, and the right layer is the output. There is only one hidden layer in this network. In a somewhat arbitrary way, 10 nodes were chosen for the hidden layer, while the number of nodes of the input and output layers can be determined from the physical properties of the problem to be solved. For the heat exchanger problem at hand, four independent parameters were fed to the input layer of the network: water-side flow rate F_w , air-side flow rate F_a , water-side inlet temperature $T_{w,in}$, and air-side inlet temperature $T_{a,in}$. The output layer of the neural network contains three parameters: the total heat transfer rate of the heat exchanger Q , the water-side temperature drop ΔT_w , and air-side temperature increase ΔT_a , which are defined as

$$\Delta T_w = T_{w,in} - T_{w,out} \quad (4.6)$$

$$\Delta T_a = T_{a,out} - T_{a,in} \quad (4.7)$$

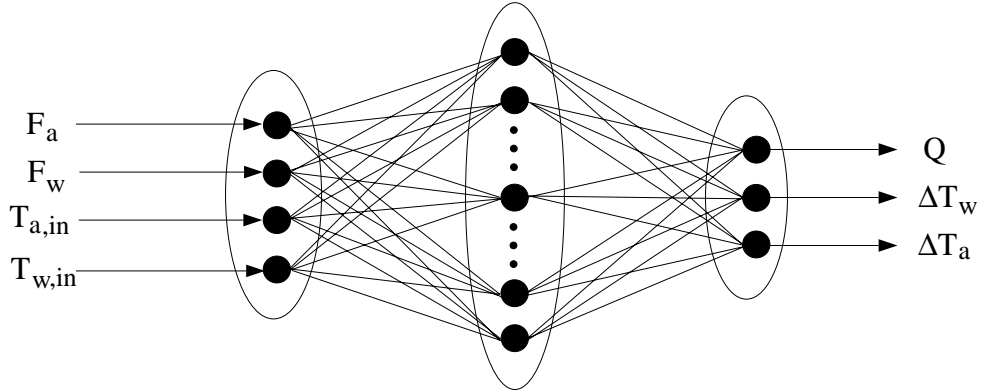


Figure 4.4: Neural network configuration used for modelling heat exchanger

A total of 259 sets of experimental data were applied to train this neural network. For the comparison to be fair, these data were exactly the same as the data used to obtain heat transfer correlations through the least-squares power-law methods. Three different water-side inlet temperatures were set for the experimental test. For each water-side inlet temperature, the varying ranges of water flow rates are listed in Table 2.1. For each fixed water flow rate, the air-side velocity V_a was also varied as shown in Table 2.1. The inlet air-side temperature was the ambient temperature, which varied from 20.0°C to 24.0°C during the time these data were being obtained.

4.4 Training Results of Neural Network

The neural network software used in this project was a program called NETS, developed by the Software Technology Branch of NASA's Johnson Space Center

(Baffes, et al., 1991). The manual for NETS is extensive so that every possible use of the program is discussed. More details about how to use NETS software can be found in the report of Voglewede (1993). One important aspect of the training process of a neural network is that changing the learning rate dynamically can accelerate the convergence of training. Experience demonstrates that giving a larger learning rate at the beginning of learning and then decreasing the learning rate as the training iteration increased can be conducive to obtaining a well-trained neural network.

The training of the neural network was terminated when the maximum relative error between the output of the network and the target output was less than 12%. Note that all of the input/output pairs were scaled in the range of 0.15 – 0.85 for training. A typical training error vs. learning cycle number is shown in Figure 4.5, where the maximum error is that between the network output and the target output. The rms error is the root mean square of the sum of the error at each output node.

The performance of the neural network in the process of correlating experimental data can be evaluated by comparing the outputs of the network with the actual training data. As an example, Figure 4.6 shows the total heat transfer rate of the heat exchanger vs. the variation of water-side Reynolds number for the water-side inlet temperature $T_{w,in} \approx 54.4^\circ\text{C}$. In this figure, the correlations of (3.11) and (3.12) have also been used. The predicted values using the trained neural network and the correlations is shown in the figure. In Figure 4.6, four sets of experimental curves are plotted corresponding respectively to four different air-side velocities. It is found that the trained neural network can

predict the heat transfer to the same accuracy as correlations obtained through the least-squares method. The errors in prediction for the neural network are less than 6% for most of the data points, and less than 12% for all of the points. On the other hand the least-squares correlation can predict heat transfer rates with a 10% error compared to experimental data.

A similar result was obtained for the prediction of the air-side temperature drop and the water-side temperature increase, which are shown in Figures 4.7–4.8 for the case of $T_{w,in} \approx 54.4^\circ\text{C}$. Again we can see that, compared to heat transfer correlations, the neural network can predict the temperature changes to the same accuracy for both water- and air-sides. For the cases of $T_{w,in} \approx 43.3^\circ\text{C}$ and $T_{w,in} \approx 65.6^\circ\text{C}$, similar results can be found, which will not be shown here.

4.5 Prediction Results of Neural Network

Once the neural network has been trained, it is expected that it can be used to predict the behavior of the heat exchanger under conditions that had not been used for training. A total of new 90 sets of experimental data were obtained for this purpose. These experimental data were obtained at two new water-side inlet temperatures. For each water flow rate, three air-side velocities were used. Additional details about the parameters are shown in Table 4.1.

The predictions of the trained neural network can be evaluated by propagating sets of test data through the network and comparing the outputs with the actual measurements. In our case, only the following parameters need to be inputted: water-side flow rate F_w , water-side inlet temperature $T_{w,in}$, air-side flow rate F_a , and air-side inlet temperature $T_{a,in}$. The outputs from the neural

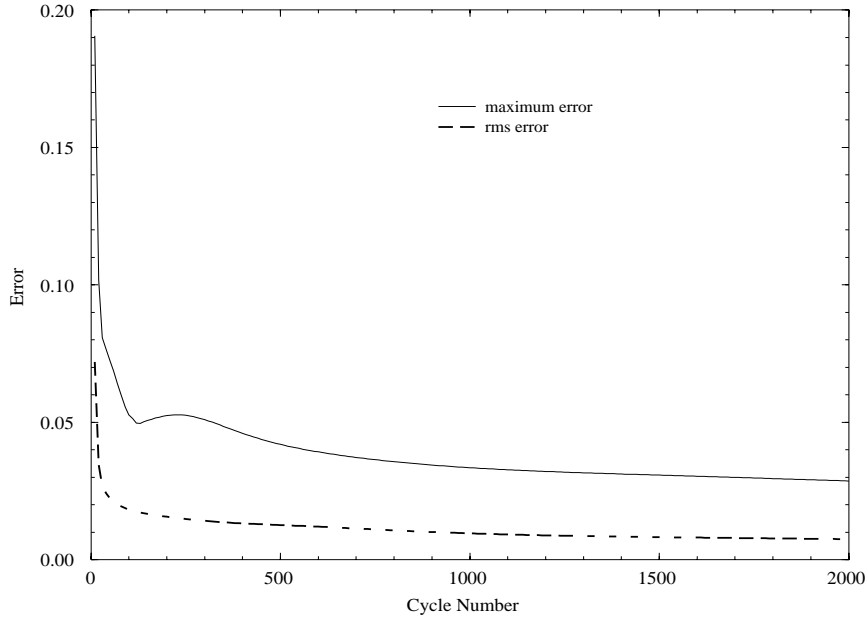


Figure 4.5: Errors of neural network via learning cycle number during training process

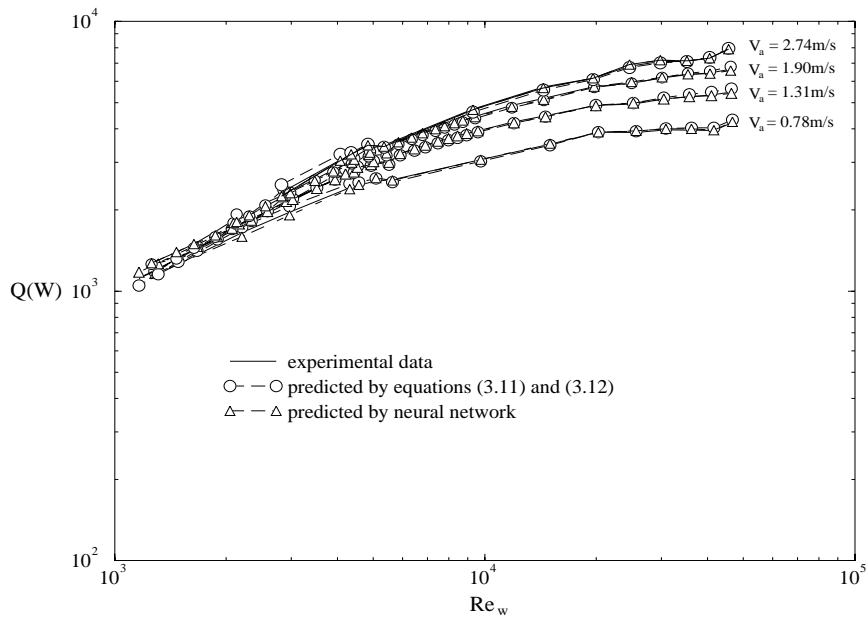


Figure 4.6: Heat transfer rates via water Reynolds number, $T_{w,in} \approx 54.4^\circ\text{C}$, data were used for obtaining correlations and training neural network

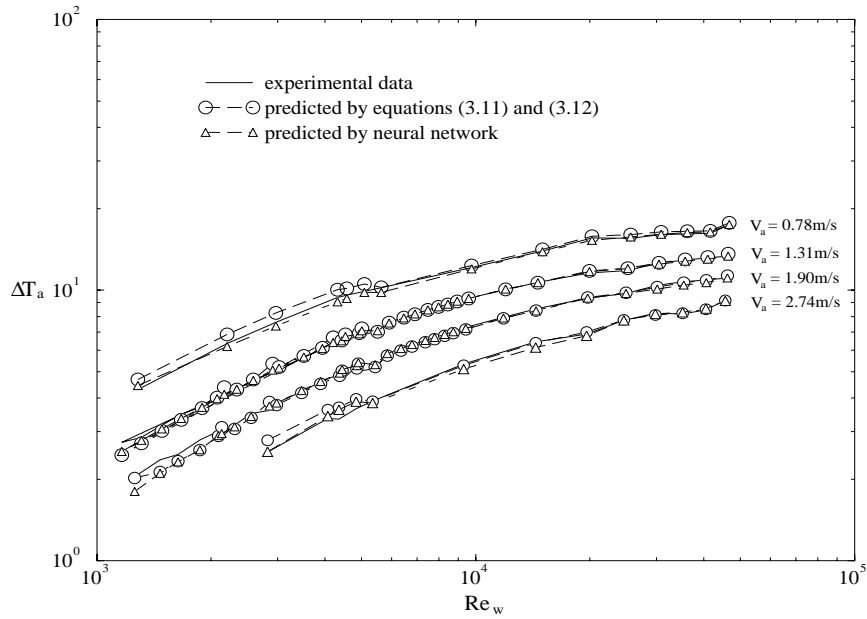


Figure 4.7: Air temperature increase via water Reynolds number, $T_{w,in} \approx 54.4^\circ\text{C}$, data were used for obtaining correlations and training neural network

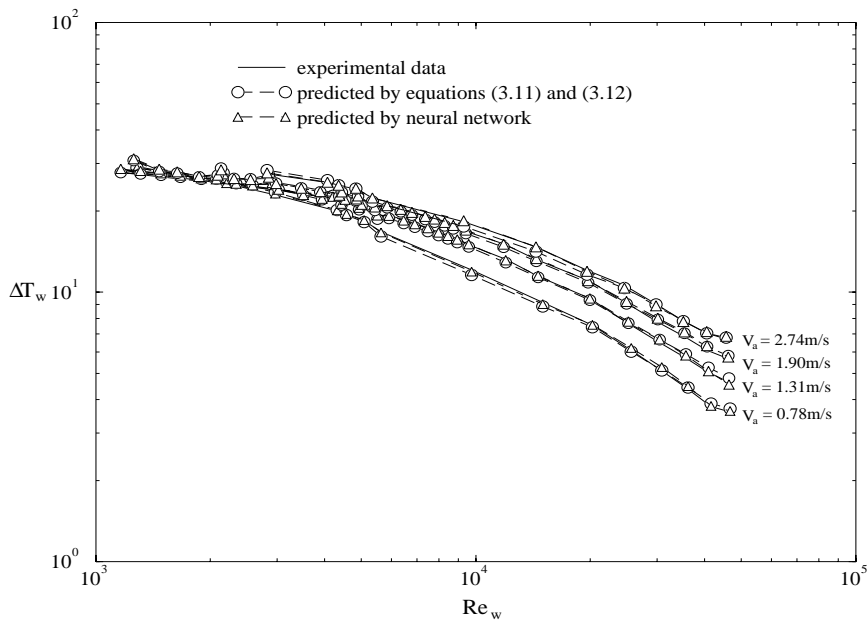


Figure 4.8: Water temperature drop via water Reynolds number, $T_{w,in} \approx 54.4^\circ\text{C}$, data were used for obtaining correlations and training neural network

Table 4.1: Testing Data

$T_{w,in}$ ($^{\circ}\text{C}$)	F_w (gpm)	V_a (m/s)
48.9	0.17–4.50	1.03, 1.61, 2.19
60.0	0.15–4.50	1.03, 1.61, 2.19

network give the following predictions: heat transfer rate Q , water-side temperature drop ΔT_w , and air-side temperature increase ΔT_a . For comparison, the power-law correlations have also been used to predict the thermal behavior of the heat exchanger for the same new data.

The results of the comparison are shown in Figure 4.9–4.14. From these figures, one finds that in the whole range of water-side Reynolds numbers, the neural network predicts the total heat transfer rates, water-side and air-side temperature changes to the same accuracy as the power-law correlations. Compared to experimental data, the prediction errors are less than 6% for most of the data and less than 12% for some data.

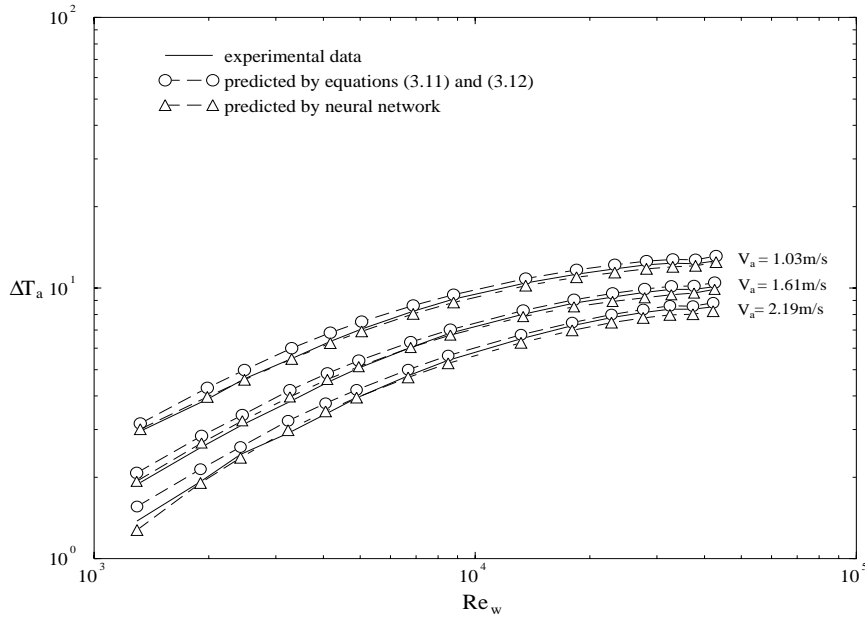


Figure 4.9: Air temperature increase via water Reynolds number, $T_{w,in} \approx 48.9^\circ\text{C}$, new data are used here for comparison

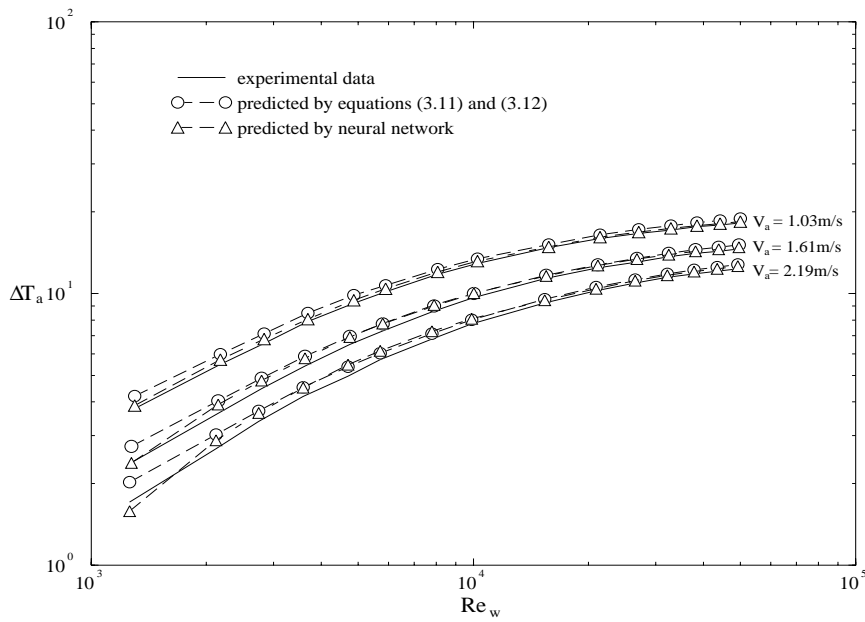


Figure 4.10: Air temperature increase via water Reynolds number, $T_{w,in} \approx 60.0^\circ\text{C}$, new data are used here for comparison

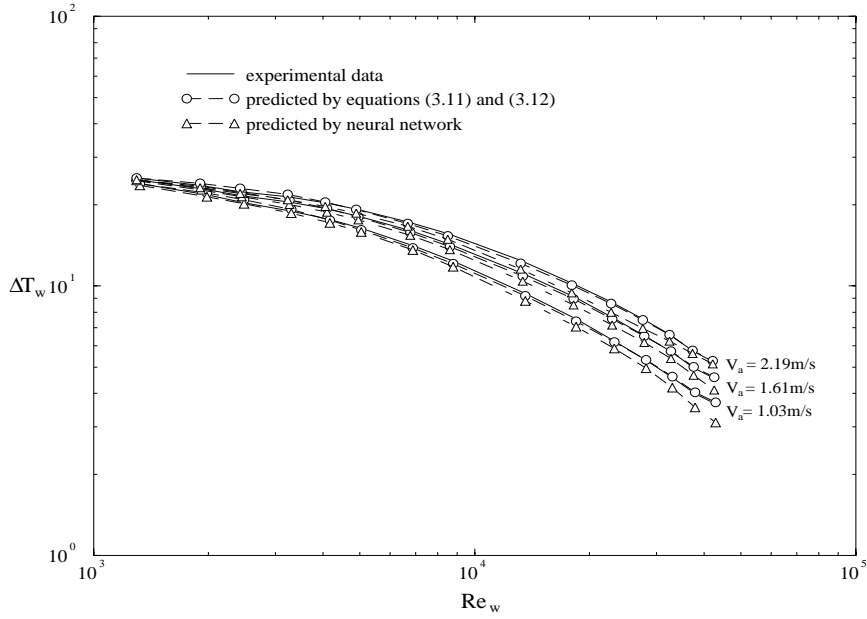


Figure 4.11: Water temperature drop via water Reynolds number, $T_{w,in} \approx 48.9^\circ\text{C}$, new data are used here for comparison

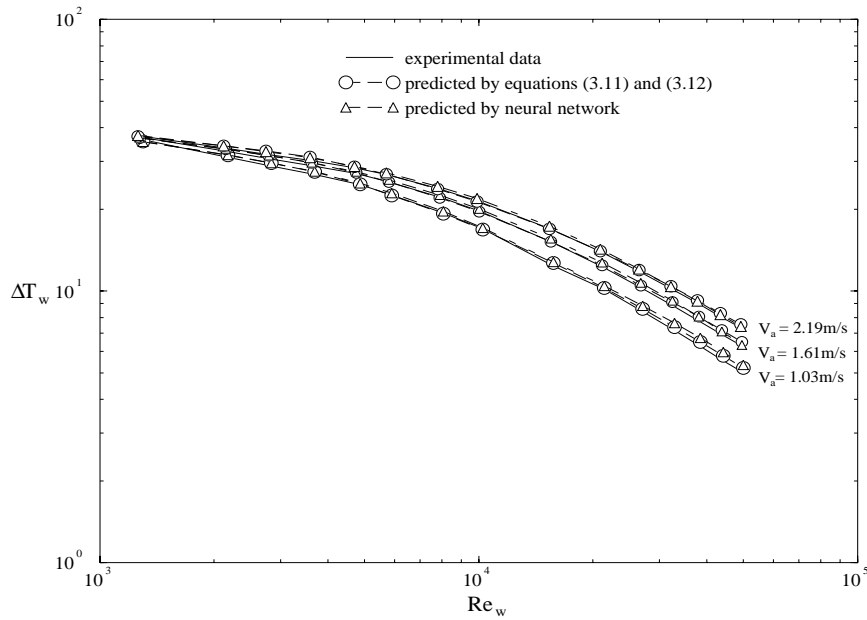


Figure 4.12: Water temperature drop via water Reynolds number, $T_{w,in} \approx 60.0^\circ\text{C}$, new data are used here for comparison

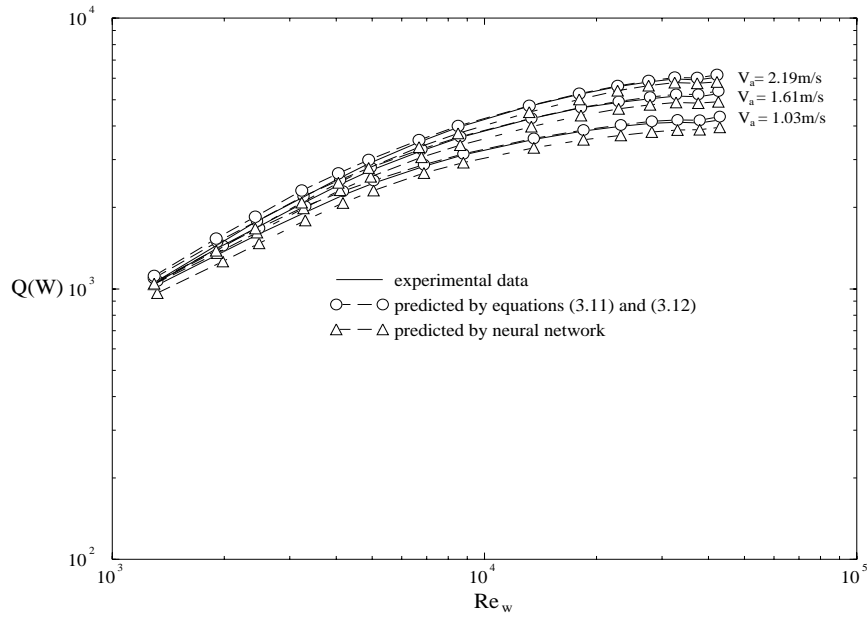


Figure 4.13: Heat transfer rates via water Reynolds number, $T_{w,in} \approx 48.9^\circ\text{C}$, new data are used here for comparison

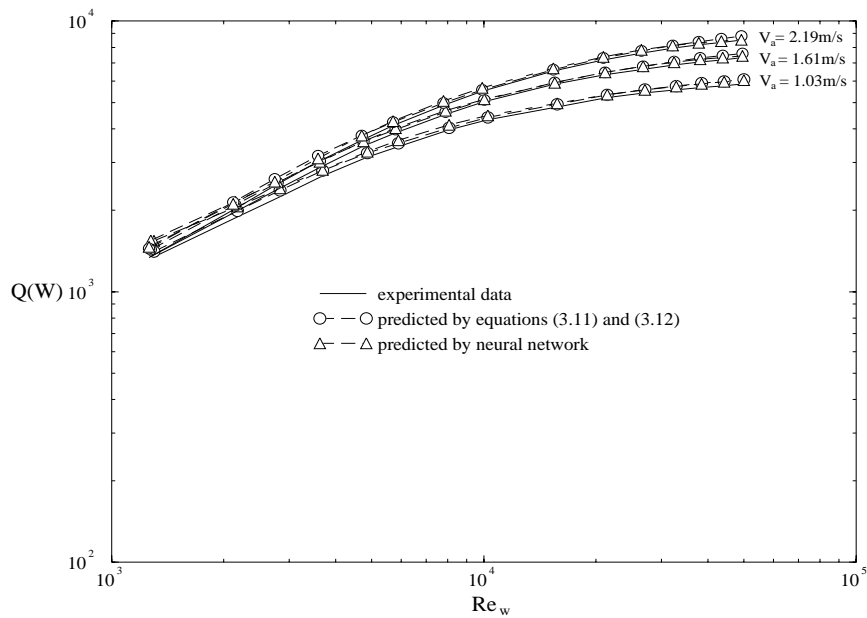


Figure 4.14: Heat transfer rates via water Reynolds number, $T_{w,in} \approx 60.0^\circ\text{C}$, new data are used here for comparison

4.6 Conclusions

The results in this chapter show that the neural network technique can be used to model the heat transfer performance of heat exchanger accurately with the added advantage that no functional relationship has to be assumed as for a correlation. A neural network once trained can be described uniquely by sets of connection weights. Our results demonstrate that a well-trained neural network predicts new heat transfer behavior with the same accuracy as conventional correlation approaches do. The main advantage of the neural network technique for modeling heat exchanger is that it can get desired output directly from a trained network without involving in the definitions of heat transfer coefficient and appropriate temperature difference. It can be anticipated that in the future, for the convenience of heat exchanger design, different type of heat exchangers will be described by different kinds of trained neural network. One can also foresee trained neural networks that can be used in a straightforward manner for the control and optimization of thermal/hydraulic system. Neural network techniques thus provide viable alternative approach for the study of heat exchangers.

CHAPTER 5

DYNAMICAL MODELING OF HEAT EXCHANGERS

5.1 Introduction

The time-dependent dynamics of a heat exchanger are very important for its control, especially in a hydronics network. In this chapter, we develop a theoretical model to simulate the thermal dynamical process of a heat exchanger. We have also carried out experiments, and the two results are compared. Qualitative agreement has been obtained though there are quantitative difference due to simplifications in the theoretical model.

5.2 Theoretical Model

We consider a single-row heat exchanger corresponding to that tested in earlier chapters for dynamical response at low water flow rates. The time-dependent thermal response of this heat exchanger can be described by using a cross flow model schematically shown in Figure 3.1.

The air-side inlet temperature T_∞ and velocity V_a are kept constant. Ini-

tially, a water-side upstream valve is completely closed so that the water downstream of the valve is static, and is at an initial temperature $T_{w,0}$. The water upstream of the valve has a constant temperature $T_{w,in}$, which is higher than $T_{w,0}$. At $t = 0$, the valve in the water line is opened. The water begins to accelerate through the tube as a result of an imposed pressure difference ΔP which provides the driving force for the motion of the water.

We will make a one-dimensional assumption and take the temperature and velocity profile across the cross-sectional area of the tube to be flat. For the moment we also neglect the thermal inertia of the tube and fin. Furthermore, the overall heat transfer coefficient, U , is taken to be constant. Under these conditions, a water-side energy balance gives

$$\frac{\partial T_w}{\partial t} + V_w(t) \frac{\partial T_w}{\partial x} = -\beta(T_w - T_\infty) \quad (5.1)$$

The coefficient β is defined by

$$\beta = \frac{Up}{\pi \rho_w c_w D_i^2 / 4} \quad (5.2)$$

where $p = A_a/L$ is the air-side average perimeter based on total air-side heat transfer area A_a

The boundary and initial conditions can be specified as

$$T_w|_{x=0} = T_{w,in}, \quad T_w|_{t=0} = T_{w,0} \quad (5.3)$$

In order to solve equations (5.1) and (5.3), we need to know $V_w(t)$. Based on momentum considerations, we have

$$\Delta P \frac{\pi D_i^2}{4} = [\rho_w \frac{\pi D_i^2}{4} L] \frac{dV_w}{dt} + \tau_0(\pi D_i L) \quad (5.4)$$

where τ_0 is the shear stress inside the tube wall. For laminar flow in a circular pipe

$$\tau_0 = \frac{8\mu}{D_i} V_w \quad (5.5)$$

Combining equations (5.4) and (5.5), and taking ΔP to be a constant, we obtain

$$V_w = V_{w,0}(1 - e^{-t/\tau_\alpha}) \quad (5.6)$$

where $V_{w,0}$ is the steady velocity that is obtained as $t \rightarrow \infty$, and τ_α is a hydrodynamic time constant defined by

$$\tau_\alpha = \frac{\rho_w D_i^2}{32\mu_w} \quad (5.7)$$

From equations (5.1), (5.3) and (5.6), we find that

$$T_w = T_\infty + (T_{w,0} - T_\infty)e^{-\beta t} \text{ for } x > x_0(t) - \tau_\alpha V_{w,0} \quad (5.8)$$

$$T_w = T_\infty + (T_{w,in} - T_\infty)f[x - x_0(t)]e^{-\beta t} \text{ for } x < x_0(t) - \tau_\alpha V_{w,0} \quad (5.9)$$

where

$$f[-x_0(t)] = e^{\beta t} \quad (5.10)$$

and $x_0(t)$ is defined by

$$x_0(t) = V_{w,0}t + \tau_\alpha V_{w,0}e^{-t/\tau_\alpha} \quad (5.11)$$

The total heat transfer rate of the heat exchanger can be determined from the water-side heat loss. Thus

$$Q(t) = \int_0^L UP(T_w - T_\infty)dx \quad (5.12)$$

which gives

$$Q(t) = UP(T_{w,in} - T_\infty)e^{-\beta t} \int_0^L f[x - x_0(t)]dx, \text{ for } t > t^* \quad (5.13)$$

and

$$\begin{aligned}
Q(t) &= UP(T_{w,0} - T_\infty)e^{-\beta t}[L - x_0(t) + \tau_\alpha V_{w,0}] \\
&+ UP(T_{w,in} - T_\infty)e^{-\beta t} \int_0^{x_0(t) - \tau_\alpha V_{w,0}} f[x - x_0(t)]dx, \text{ for } t < t^* \quad (5.14)
\end{aligned}$$

t^* is the solution of

$$L = V_{w,0}t + \tau_\alpha V_{w,0}(e^{-t/\tau_\alpha} - 1) \quad (5.15)$$

The air-side outlet temperature can be determined from a balance between the air-side heat gain and the water-side heat loss. We can neglect the air-side thermal inertia since the density and specific heat of air are small. Thus, we have

$$T_{a,out} = T_\infty + \frac{Q(t)}{\rho_a c_a F_a} \quad (5.16)$$

where F_a is the air-side flow rate.

5.3 Experiments

Laboratory experiments have also been performed to obtain dynamical response data for the heat exchanger. Tests were carried out with the air-side face velocity kept at a constant value of 1.03 m/s, and the water-side inlet temperature at 48.9°C. Before each test, the water-side flow rate was made zero by closing the upstream valve. After a while the initial temperature distribution of the water was uniform everywhere and equal to the air-side inlet temperature T_∞ . The upstream valve was then suddenly opened and the time history of the air-side outlet temperature recorded.

The final steady-state water-side flow rate could be adjusted by opening the valve to a desired position. On reaching steady state this flow rate was measured

by the flow meter. Three different steady water-side flow rates have been used for the dynamical measurements.

5.4 Results and Discussion

Comparison between the theoretical predictions and experimental data for the air-side outlet temperature are shown in Figures 5.1–5.3. The steady-state water flow rates, F_w , and the non-dimensional temperature for the air-side have been shown, where the non-dimensional temperature is defined as

$$\theta_a = \frac{T_{a,out} - T_\infty}{T_{a,s} - T_\infty} \quad (5.17)$$

where $T_{a,s}$ is the steady air-side outlet temperature that is reached when $t \rightarrow \infty$.

It is seen from these figures that the theoretical predictions have trends qualitatively similar to those of the experiments. This implies that the relatively simple theoretical model captures some of the important physical characteristics of the process. Quantitatively, however, there is still some difference between the two results. The model always shows a much faster dynamical response than the experiment data. It is believed that the main reason for this is the neglect of the thermal inertia of the tube and fins in the model. The large mass of the metal would slow down the response considerably and bring it into closer agreement with observations.

The variation of water-side outlet temperature with time is shown in Figure 5.4. A non-dimensional temperature defined by

$$\theta_w = \frac{T_{w,out} - T_{w,0}}{T_{w,s} - T_{w,0}} \quad (5.18)$$

has been used for water-side, where $T_{w,s}$ is the steady water-side outlet temperature. No experimental data have been obtained for this temperature.

All the previous results have been obtained by setting the water-side initial temperature $T_{w,0}$ equal to the air-side inlet temperature T_∞ . It is interesting to see what happens if these two temperatures are not equal. Figure 5.5 shows the variation of air-side outlet temperature with time predicted by the model for the case of $T_{w,0} - T_\infty = 10^\circ\text{C}$. It is found that the air-side outlet temperature decreases first to a minimum before increasing continuously to a steady value.

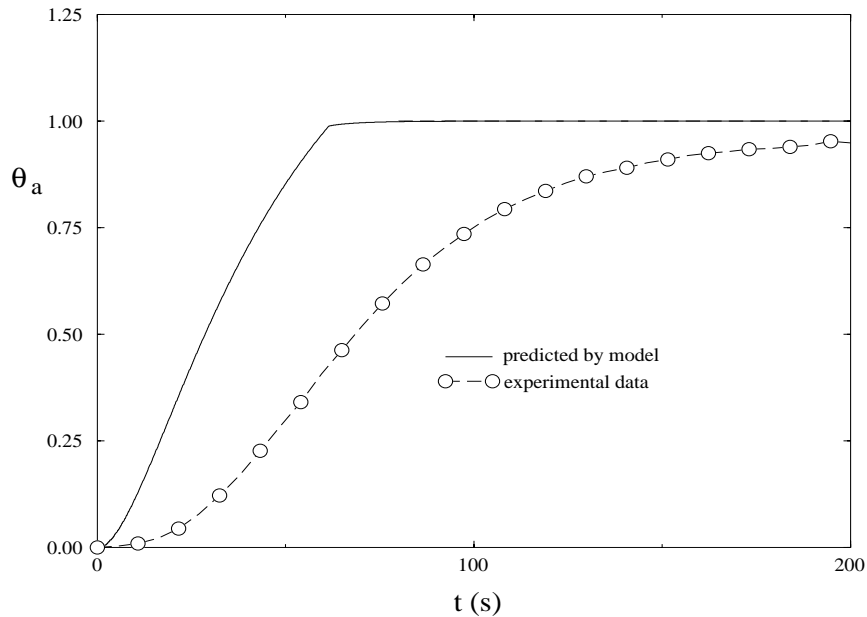


Figure 5.1: Variation of air-side outlet temperature with time, $F_w = 0.39$ gpm, $T_{w,0} = T_\infty$

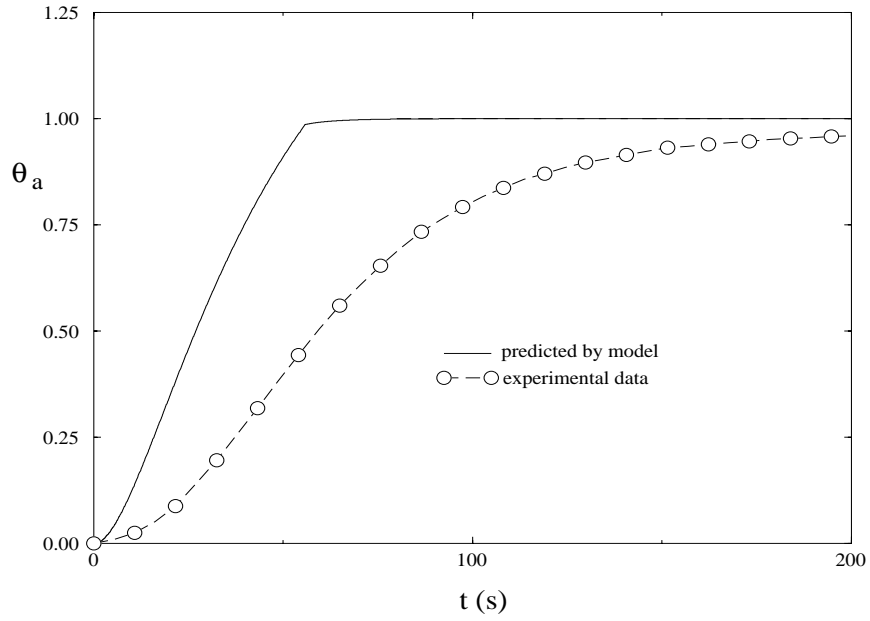


Figure 5.2: Variation of air-side outlet temperature with time, $F_w = 0.44$ gpm,
 $T_{w,0} = T_\infty$

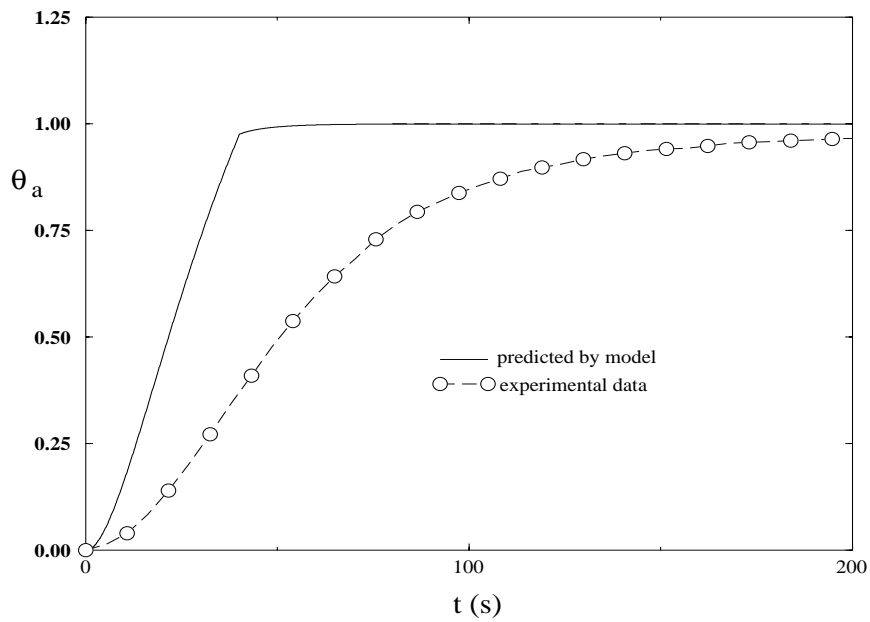


Figure 5.3: Variation of air-side outlet temperature with time, $F_w = 0.66$ gpm,
 $T_{w,0} = T_\infty$

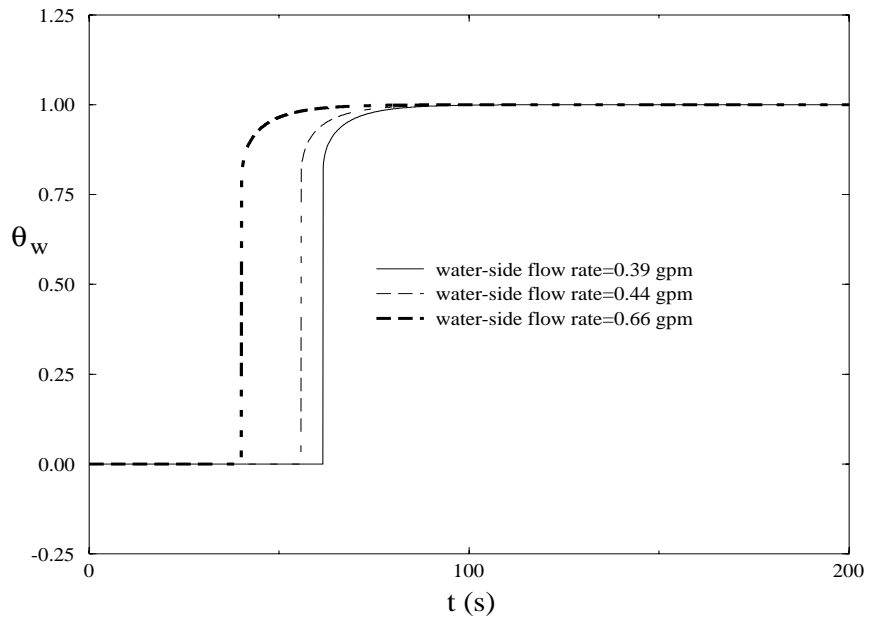


Figure 5.4: Variation of water-side outlet temperature with time, $T_{w,0} = T_\infty$

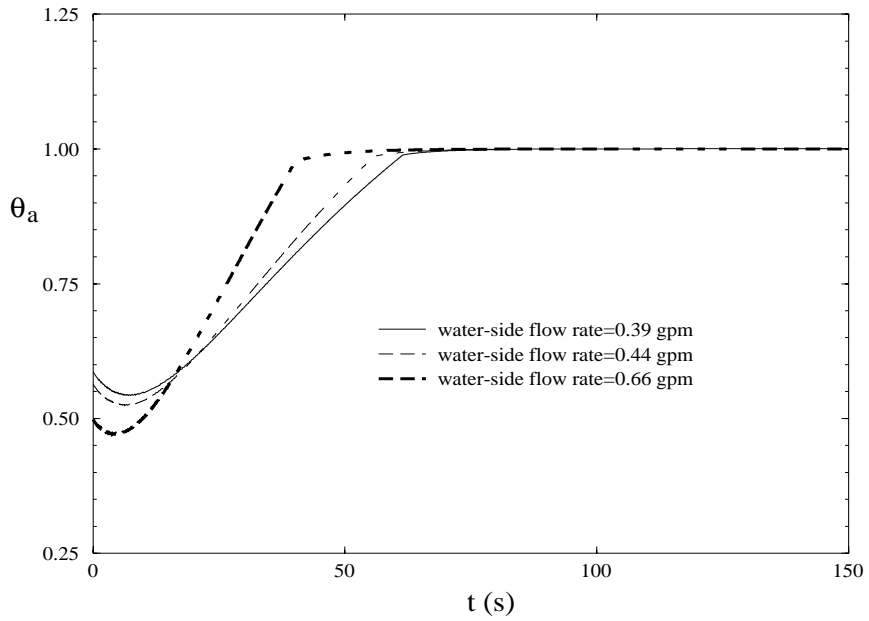


Figure 5.5: Air-side outlet temperature variation with time, $T_{w,0} - T_\infty = 10^\circ\text{C}$

5.5 Conclusions

A simple theoretical model has been presented in this chapter for simulating the dynamical response of a heat exchanger. The predictions of the model have been compared with experimental data. The comparison shows that this simple model can catch some of the physical features of the time-dependent behavior of the heat exchanger. Quantitatively, however, there is some difference between the predictions of the model and experimental results. This is perhaps due to the thermal inertia of the tube and fins which has been neglected.

It is important to note the time scale of the heat exchanger response. The particular heat exchanger tested responds in about a minute or so. This value should be quite typical. The issue is important, not so much for itself, but in the context of control of outlet temperatures. It is fairly complicated when a network is involved, as the different branches as well as the different components may have different speeds of response. The purpose of the modeling is not so much to understand heat exchanger behavior, but to be able to have dynamically tested model equations that can eventually be used to simulate and control a hydronic network.

CHAPTER 6

CONCLUSIONS AND RECOMMENDATIONS

6.1 Conclusions

Chapters 2 through 5 of this thesis describe different aspects of the research project on the hydronics of low-flow coils. Specifically we have concentrated on the single-row heat exchanger as a simple example. Here we summarize some of the most significant items that have been learned so far:

1. A least-squares power-law method has been developed for the reduction of experimental data to heat transfer correlations on both the water- and air-sides.
2. Another method based on artificial neural networks, that may have some advantages in some applications, is also developed.
3. The logarithmic mean temperature difference method that is sometimes used is found to be deficient for the single-row coil. An alternative based on first principles is offered.

4. Suitable heat transfer correlations on the water- and air-sides for the specific heat exchanger tested have been determined. It is found that the secondary flow induced by the bends strongly influences the over all heat transfer.
5. A preliminary analysis of the dynamic response of a heat exchanger to a suddenly-imposed pressure drop under laminar flow conditions has been carried out, and the results show a qualitative agreement with the experimental data for a single-row fin-tube heat exchanger. The quantitative discrepancy of the two results appears to be due to the neglect of the thermal inertia of the fins and tubes in the model.

6.2 Recommendations

1. Different heat exchangers should be chosen for heat transfer test at low flow rates so that the effects of fin spacing, number of tube rows, fin pitch, bend dimension and other geometrical parameters can be concerned.
2. Based on the experimental data of different heat exchangers, general heat transfer correlations at low flow rates for both water-side and air-side should be correlated, in which the above geometrical effects should be taken into account.
3. The bend effect on heat transfer in a straight pipe downstream the bend for laminar flow should be examined in detail based on numerical simulation.
4. More sophisticated dynamical models should be applied to simulate the dynamical response of heat exchangers.

BIBLIOGRAPHY

- [1] ARI. 1987. *ARI Standard 410-87, Forced-circulation air-cooling and air-heating coils*. Arlington, VA: Air-Conditioning and Refrigeration Institute.
- [2] Baffes T.P., R.O. Shelton and T.A. Phillips, 1991, NETS User's Guide, *Software Technology Branch, Lyndon B. Johnson Space Center*
- [3] Batill S.M. 1994. Experimental uncertainty and drag measurements in the National Transonic Facility, *Hessert Center for Aerospace Research, University of Notre Dame*
- [4] Bhat, N. V., P.A., Minderman, Jr., T. McAvoy and N. Sun Wang, 1992, *Modeling chemical process system via neural computation*, Neural Networks, Current applications, edited by P.G.J. Lisboa, Chapman & Hall, London
- [5] Cheng, K C., Yuen, F P., 1987. Flow visualization studies on secondary flow patterns in straight tubes downstream of a 180 deg bend and in isothermally heated horizontal tubes, *ASME J. Heat Transfer*, **109**:49-54.
- [6] Colburn, A.P. 1933. A method of correlating forced convection heat transfer data and a comparison with fluid friction, *AIChE Trans.*, **29**:174.
- [7] Croall I.F. and Mason L.P. (Eds.), 1991, *Industrial Applications of Neural Networks, Research Reports ESPRIT, Project 2092· ANNIE·*, **1**, Springer-Verlag, Berlin
- [8] Cybenko G., 1989, Continuous value neural networks with two hidden layers are sufficient, *Math. Contr. Signal & Sys.*, **2**:303-314.
- [9] Dayhoff E.J., 1990, *Neural Network Architectures: an introduction*, Van Nostrand Reinhold, New York
- [10] Dittus, F.W. and L.M.K. Boelter. 1930. Heat transfer in automobile radiators of the tubular types, *University of California Publication Engineering*, **12**:443.
- [11] Ede, A.J. 1966. The effect of a 180° bend on heat transfer to water in a tube. *3rd Int. Heat Transfer Conference*, Chicago, **1**:99-103.

- [12] Faller E.W., S.J. Schreck and M.W. Luttges, 1994, Real-time prediction and control of three-dimensional unsteady separated flow fields using neural network, *submitted to J. Aircraft*
- [13] Fan X., L. Hofmann and T. Herbert, 1993, Active flow control with neural network, *AIAA Shear Flow Conference*, AIAA-93-3273, July 6-9, Orlando, Florida
- [14] Figliola S.R. and D.E. Beasley. 1991. *Theory and design for mechanical measurements*, New York: John Wiley & Sons. Inc.
- [15] Geladi, P. and Kowalski, B., 1986, Partial least squares regressions: a tutorial, *Anal. Chim. Acta*, **185**:1-17.
- [16] Gnielinski, V. 1976. New equation for heat and mass transfer in turbulent pipe and channel flow, *Int. Chem. Eng.*, **16**(2):359-368.
- [17] Haan L. Fred,Jr., R.J. Minniti,III, and X. Zhao, 1994, Flow control using neural network, *Department of Aerospace and Mechanical Engineering, University of Notre Dame*
- [18] Idem, S.A., A.M. Jacobi and V.W. Goldschmidt. 1990. Heat transfer characterization of a finned-tube heat exchanger (with and without condensation), *J. Heat Transfer*, **112**:64-70.
- [19] Idem, S.A., C. Jung, G.G. Gonzalez and V.W. Goldschmidt. 1987. Performance of air-to water copper finned-tube heat exchanger at moderately low air-side Reynolds number, including effects of baffles, *Int. J. Heat Mass Transfer*, **30**(8):1733-1741.
- [20] Incropera, F., and DeWitt, D. 1992. *Heat transfer*, 6th ed., New York: McGraw-Hill.
- [21] Jacobson A. S. and W.C. Reynolds, 1993, Active control of boundary layer wall shear stress using self-learning neural network, *AIAA Shear Flow Conference*, AIAA-93-3272, July 6-9, Orlando, Florida
- [22] Kalb C.E. and Seader J.D., 1974. Fully developed viscous-flow heat transfer in curved circular tubes with uniform wall temperature. *AIChE Journal*, **20**:340-346.
- [23] Kayansayan, N., 1993. Heat transfer characterization of flat plain fins and round tube heat exchangers. *Experimental Thermal and Fluid Science*, **6**:263-272.
- [24] Kays, W.M. and A.L. London. 1984. *Compact Heat Exchangers*, New York: McGraw-Hill Book Company, 3rd ed.

- [25] Kline, S.J. and F.A. McClintock. 1953. Describing uncertainties in single-sample experiments, *Mech. Eng.*, **75**:3-8.
- [26] Lis J. and Thelwell, M.J. 1963-1964. Experimental investigation of turbulent heat transfer in a pipe preceded by a 180 deg bend. *Proc. Inst. of Mech. Engrs.*, **178**(31):17-25.
- [27] Lisboa, P.G.J., 1992, *Neural Networks: current applications*, Chapman & Hall, London
- [28] Lippmann, R.P., 1987, An introduction to computing with neural nets. *IEEE ASSP Magazine*, **4**(2):4-22.
- [29] Lombardi C., Marseguerra M. and Zio E., 1994, Thermalhydraulic correlations by neural networks. *Proceedings of the Tenth International Heat Transfer Conference*, Brighton, UK. **2**:391-396.
- [30] McQuiston, F.C. 1981. Finned tube heat exchangers: state of the art for the air-side. *ASHRAE Trans.*, **87**(1):1077-1085.
- [31] Mehta, N.D. and Bell, K.J. 1981. Laminar flow heat transfer in a tube preceded by a 180° bend. *Heat Transfer-Soviet Research*, **13**(6):71-80.
- [32] Mirth, D.R., Ramadhyani, S. and Hittle, D.C. 1993. Thermal performance of chilled-water cooling coils operating at low water velocities, *ASHRAE Trans.*, **99**(1):43-53.
- [33] Moshfeghian, M. and Bell, K.J. 1979. Local heat transfer measurements in and downstream from a U-bend. *ASME paper*, No. 79-HT-82.
- [34] Nelson, Marilyn McCord, and W.T. Illingworth, 1991, *A Practical Guide to Neural Nets*, Addison-Wesley, Reading, Mass.
- [35] Petukhov, B.S. 1970. Heat transfer and friction in turbulent pipe flow with variable physical properties, *Advances in Heat Transfer*, **6**:503-564.
- [36] Shah, R.K. and Joshi, S.D. 1987. Convective heat transfer in curved ducts. In *Handbook of Single-Phase Convective Heat Transfer*, Eds. S. Kakac, R.K. Shah, W. Aung, John Wiley, New York.
- [37] Shepherd, D. G., 1956. Performance on one-row tube coils with thin-plate fins, low velocity forced convection. *Heating, Piping & Air Conditioning*, April, 137-144.
- [38] Sieder, E.N. and C.E. Tate. 1936. Heat transfer and pressure drop of liquids in tubes, *Ind. Eng. chem.*, **28**:1429.

- [39] Stevens, R.A., J. Fernandez, and J. Woolf. 1957. Mean Temperature Difference in One-, Two- and Three-pass Crossflow Heat Exchangers”, *ASME Trans.* **79**:287-297.
- [40] Tailby, S.R. and Staddon, P.W. 1970. The influence of 90° and 180° pipe bends on heat transfer from an internally flowing gas stream. *4th Int. Heat Transfer Conference*, Paris-Versailles, 2:FC4.5
- [41] Thibault J. and B.P.A. Grandjean, 1991, A neural network methodology for heat transfer data analysis, *Int. J. Heat Mass Transfer*, **34**:2063-2070.
- [42] Voglewede A.P., 1993, Integration of neural network into optimization routines, *Department of Aerospace and Mechanical Engineering, University of Notre Dame*
- [43] Welstead, S.T., 1992, Neural network modeling of chaotic dynamics in nuclear reactor flows, *Trans. of the American Nuclear Society*, **65**:210-211.
- [44] Wilson, E.E., 1915, Basis for rational design of heat transfer apparatus. *ASME Trans.* **37**:47-82.

APPENDIX-A: UNCERTAINTY ANALYSIS

.1 Error Sources

Based on water-side's heat loss, the total heat transfer rate, Q , from the heat exchanger can be determined experimentally through measuring water flow rate F_w , water inlet temperature $T_{w,in}$ and water outlet temperature $T_{w,out}$ and using equation (3.4):

$$Q = \rho_w F_w c_{pw} (T_{w,in} - T_{w,out}) \quad (.1)$$

Examining the above equation, one can find that the error sources for the heat transfer result come from the measurements of water-side temperatures and water flow rate. Usually, experimental errors can be grouped into two very general categories: precision error and bias error. Precision error comes from the scatter of data in multiple measurements. It can be determined through statistical analysis of the data from the multiple measurement. Unlike the precision error, the bias error comes from the following sources:

- calibration error
- data acquisition error
- data reduction error

For the problem concerned here, the error sources and uncertainty analysis flow chart is shown in Figure .1.

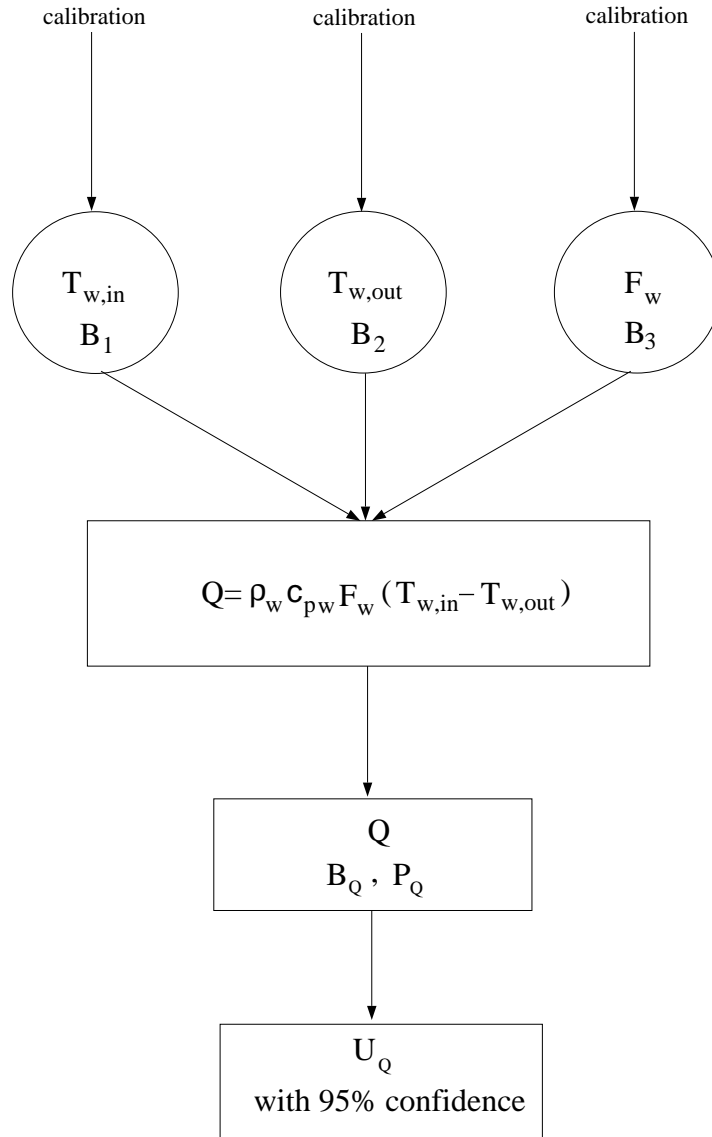


Figure .1: Schematic of uncertainty analysis

.2 Data Reduction and Uncertainty Analysis

.2.1 Curve fitting

Curve fitting is a data processing procedure in which the basic concepts of propagation of errors or statistical analysis can be applied in order to estimate the required uncertainty information. We only consider the least square curve fit here which will be used to quantify a linear relationship between X and Y and provide the slope, m , and intercept, a , for the expression:

$$Y = mX + a \quad (.2)$$

For linear polynomials fit, the following expressions can be used for the calculation of m and a (Batill, 1994)

$$m = \frac{N \sum_{i=1}^N X_i Y_i - \sum_{i=1}^N X_i \sum_{i=1}^N Y_i}{N \sum_{i=1}^N X_i^2 - [\sum_{i=1}^N X_i]^2} \quad (.3)$$

$$a = \frac{\sum_{i=1}^N X_i^2 \sum_{i=1}^N Y_i - \sum_{i=1}^N (X_i Y_i) \sum_{i=1}^N X_i}{N \sum_{i=1}^N X_i^2 - [\sum_{i=1}^N X_i]^2} \quad (.4)$$

A correlation coefficient, γ , can be defined by (Figliola and Beasley, 1991)

$$\gamma = \sqrt{1 - \frac{S_{Y_i}}{S_Y}} \quad (.5)$$

where S_{Y_i} is the precision index for the dependent variable, which can be expressed as

$$S_{Y_i} = \left[\frac{\sum_{i=1}^N (Y_i - a - m X_i)^2}{N - 2} \right]^{\frac{1}{2}} \quad (.6)$$

and S_Y is defined as

$$S_Y^2 = \frac{1}{N - 1} \sum_{i=1}^N (Y_i - Y)^2 \quad (.7)$$

The correlation coefficient represents a quantitative measure of the linear association between X and Y .

The estimates of the precision indices for a and m can be given by

$$S_a = \left[\sum_{i=1}^N \left(\frac{\partial a}{\partial Y_i} S_{Y_i} \right)^2 \right]^{\frac{1}{2}} S_m = \left[\sum_{i=1}^N \left(\frac{\partial m}{\partial Y_i} S_{Y_i} \right)^2 \right]^{\frac{1}{2}} \quad (.8)$$

Once the two estimates of the precision limits for the parameters a and m have been determined, these parameters are ‘frozen’ until the next time a calibration is conducted. They become bias errors.

.2.2 Bias errors due to calibration

In the case of calibration experiment, the independent variable, x , is usually the value of the working standard and is often expressed as a quantity in engineering units. The dependent variable, y , is the sensor output often expressed as volts. When the calibration experiment is complete, the curve fit performed and the uncertainties computed, the instrument is now used in a measurement. When this occurs, we have the following expression,

$$X_M = A + MY \quad (.9)$$

where X_M is the measured parameter in engineering units corresponding to the voltage Y . The slope and intercept for this reciprocal relation are

$$A = -\frac{a}{m}M = \frac{1}{m} \quad (.10)$$

Since A and M are the results of computations using the values of a and m , one can estimate the precision index for A and M from the precision index for a and m by using the expressions

$$S_A = \left[\left(\frac{\partial A}{\partial a} S_a \right)^2 + \left(\frac{\partial A}{\partial m} S_m \right)^2 \right]^{\frac{1}{2}} \quad (.11)$$

$$S_M = \left[\left(\frac{\partial M}{\partial a} S_a \right)^2 + \left(\frac{\partial M}{\partial m} S_m \right)^2 \right]^{\frac{1}{2}} \quad (.12)$$

Evaluating these two expression yields

$$S_A = \left[\left(\frac{S_a}{m} \right)^2 + \left(\frac{a}{m^2} S_m \right)^2 \right]^{\frac{1}{2}} \quad (.13)$$

and

$$S_M = \frac{S_m}{m^2} \quad (.14)$$

Then in the process of using the calibration constants to evaluate the “measured” parameter X_M , the precision limit from the “curve fit” is “frozen” as a bias limit since A and M are fixed parameters. Combining with other bias sources, the bias limits in A and M can be computed by addition in quadrature

$$B_A = \left[(B_{curve\ fit})^2 + (B_{WS})^2 + (B_{other})^2 \right]^{\frac{1}{2}} B_M = \left[(B_{curve\ fit})^2 + (B_{other})^2 \right]^{\frac{1}{2}} \quad (.15)$$

The above equations are based on the assumption that the biases in the curve-fitting and calibration process are uncorrelated.

Then the bias in X_M due to the propagation of bias from A , M and Y can be determined by

$$B_{X_M} = \left[\left(\frac{\partial X_M}{\partial A} B_A \right)^2 + \left(\frac{\partial X_M}{\partial M} B_M \right)^2 + \left(\frac{\partial X_M}{\partial Y} B_Y \right)^2 \right]^{\frac{1}{2}} \quad (.16)$$

which results in the expression

$$B_{X_M} = \left[(B_A)^2 + (M B_Y)^2 + (Y B_M)^2 \right]^{\frac{1}{2}} \quad (.17)$$

.2.3 Propagation of uncertainty to results

Consider the result, r , which is determined through the functional relationship between the measured variables P_1, P_2, \dots, P_j as defined by the following

equation

$$r = r(P_1, P_2, \dots, P_j) \quad (.18)$$

The propagation of precision error and bias error through the variables to the result can be determined by

$$S_r = \left[\sum_{i=1}^j (\theta_i S_{P_i})^2 \right]^{\frac{1}{2}} B_r = \left[\sum_{i=1}^j (\theta_i B_{P_i})^2 \right]^{\frac{1}{2}} \quad (.19)$$

where θ_i are the “sensitivities” of the result to variations in each parameter P_i defined by

$$\theta_i = \frac{\partial r}{\partial P_i} \quad (.20)$$

This expression should be evaluated at the appropriate nominal values of the parameters, P_i .

Once both the bias limit, B_r , and the precision index, S_r , and associated “ t ” factor for the result have been determined for a particular test point or set of test conditions, the bias and precision errors can be combined in a quadrature way to give the final uncertainty result

$$U_r = [B_r^2 + (tS_r)^2]^{\frac{1}{2}} \quad (.21)$$

The t value in the above equation dependent on the degree of freedom in the result, the Welch-Satterthwaite formula can be used to determine this degree of freedom (Figliola and Beasley, 1991)

$$\nu_r = \frac{\left[\sum_{i=1}^j (\theta_i S_{P_i})^2 \right]^2}{\sum_{i=1}^j \left[(\theta_i S_{P_i})^4 / \nu_{P_i} \right]} \quad (.22)$$

Typically, the “ t ” factor is chosen for a 95% coverage, which gives the uncertainty for 95% coverage. This allows a statement for the result in a form

$$r \pm U_r \quad (95\% \text{ confidence level}) \quad (.23)$$

.3 Sample Calculation

.3.1 Calibration results

Using curve fitting equations (.3) and (.4), the calibrated data for thermocouples can be correlated as linear relation function. For thermocouple 1, we have

$$V_1(\text{mv}) = 0.042287T_1(^{\circ}\text{C}) - 0.0684436, \quad \gamma = 0.9998 \quad (.24)$$

The precision index for the slope and intercept can be determined by using equations (.8) and (.8) respectively

$$S_{a_1} = 0.00707\text{mv}, \quad S_{m_1} = 0.00015\text{mv}/^{\circ}\text{C} \quad (.25)$$

For thermocouple 2, we have

$$V_2(\text{mv}) = 0.042299T_2(^{\circ}\text{C}) - 0.0693248, \quad \gamma = 0.9998 \quad (.26)$$

and

$$S_{a_2} = 0.007036\text{mv}, \quad S_{m_2} = 0.000149\text{mv}/^{\circ}\text{C} \quad (.27)$$

For the flow sensor, the relation between the voltage output from the flow meter and the flow rate passing through the meter can be correlated as the following linear relation from calibration data

$$V_F(\text{v}) = 1.10764F_w(\text{gpm}) + 0.030431, \quad \gamma = 0.9992 \quad (.28)$$

and

$$S_{a,F} = 0.0254\text{v}, \quad S_{m,F} = 0.0107\text{v}/\text{gpm} \quad (.29)$$

.3.2 Calibration error

For thermocouple 1, from equations (.10) and (.10), we have

$$T_1 = 23.648V_1 + 1.619 \quad (.30)$$

From equations (.11) and (.12), we have the precision index for the slope and intercept of the above expression

$$S_A = 0.167^\circ\text{C}, \quad S_M = 0.080(^\circ\text{C}/\text{mv}) \quad (.31)$$

The work standard error B_{WS} for the calibration of thermocouple comes from the reading error from the thermometer. For our case, we have $B_{WS} = 0.05^\circ\text{C}$. From equations (.15) and (.15), we have

$$\begin{aligned} B_A &= [(B_{curve\ fit})^2 + (B_{WS})^2]^{\frac{1}{2}} \\ &= 0.174^\circ\text{C} \end{aligned} \quad (.32)$$

$$\begin{aligned} B_M &= [(B_{curve\ fit})^2]^{\frac{1}{2}} \\ &= 0.080^\circ\text{C}/\text{mv} \end{aligned} \quad (.33)$$

For air-side velocity $V_a=1,90$ m/s, water-side flow rate $F_w=0.50$ gpm, using the calibrated thermocouples, we measured the mean water-side inlet temperature and mean water-side outlet temperature, which are: $T_{w,in} = 53.70^\circ\text{C}$ and $T_{w,out} = 30.55^\circ\text{C}$. The mean voltage output from thermocouple 1 is $V = 2.202\text{mv}$. The bias error of V is, $B_V = 0.001\text{mv}$. So using equation (.17), we have the bias error for water inlet temperature

$$\begin{aligned} B_{T_{w,in}} &= [(B_A)^2 + (VB_M)^2 + (MB_V)^2]^{\frac{1}{2}} \\ &= 0.248^\circ\text{C} \end{aligned} \quad (.34)$$

.3.3 Precision error

The precision error for water inlet temperature is due to the repeated measurement of this temperature. We took $N = 20$ measurements for each measured parameter during a steady state. For this sample experimental data, we have $S_{T_{w,in}} = 0.35^\circ\text{C}$, then the precision error of the mean water inlet temperature is

$$\begin{aligned} S_{\bar{T}_{w,in}} &= \frac{S_{T_{w,in}}}{\sqrt{N}} \\ &= 0.08^\circ\text{C} \end{aligned} \quad (.35)$$

.3.4 Uncertainty in heat transfer

For our sample data, the total heat transfer rate from the coil can be calculated by using equation (1), which gives $Q = 3025.9(\text{W})$. The water-side Reynolds number is $Re_w = 4211.1$

From equation (.19), we can calculate the precision error of total heat transfer rate

$$\begin{aligned} S_Q/Q &= \left[\left(\frac{S_{F_w}}{F_w} \right)^2 + \left(\frac{S_{T_{w,in}}}{T_{w,in} - T_{w,out}} \right)^2 + \left(\frac{S_{T_{w,out}}}{T_{w,in} - T_{w,out}} \right)^2 \right]^{\frac{1}{2}} \\ &= 3.0\% \end{aligned} \quad (.36)$$

Similarly, from equation (.19), the bias error of total heat transfer rate can be determined as

$$\begin{aligned} B_Q/Q &= \left[\left(\frac{B_{F_w}}{F_w} \right)^2 + \left(\frac{B_{T_{w,in}}}{T_{w,in} - T_{w,out}} \right)^2 + \left(\frac{B_{T_{w,out}}}{T_{w,in} - T_{w,out}} \right)^2 \right]^{\frac{1}{2}} \\ &= 2.5\% \end{aligned} \quad (.37)$$

The degrees of freedom in the Q can be determined by equation (.22), which gives the result as $\nu_Q \approx 24$, so the t value for 95% confidence level is $t = 2.06$.

Combining the precision error and bias error through using equation (.21), we can get the total uncertainty in Q

$$\begin{aligned} U_Q &= [B_Q^2 + (tS_Q)^2]^{\frac{1}{2}} \\ &= 201.7\text{W} \end{aligned} \tag{.38}$$

or

$$U_Q/Q = 6.6\% \tag{.39}$$

So the measured value of heat transfer rate can be interpreted as:

$$Q = 3025.9 \pm 201.7 \text{ W} \tag{.40}$$

APPENDIX-B: LEAST-SQUARES APPROACH

The total thermal resistance of the heat exchanger is the sum of the thermal resistances of air-side and water-side:

$$\frac{1}{UA_a} = \frac{1}{\eta h_a A_a} + \frac{1}{h_w A_w} \quad (.41)$$

assuming

$$\eta Nu_a = a_1 Re_a^m Pr_a^{1/3} \quad (.42)$$

$$Nu_w = b_1 Re_w^n Pr_w^{0.3} \quad (.43)$$

where Nu_a and Nu_w are defined as

$$Nu_a = \frac{h_a \delta}{k_a} \quad (.44)$$

$$Nu_w = \frac{h_w D_i}{k_w} \quad (.45)$$

let

$$y = \frac{1}{U} \quad (.46)$$

then from equations (.41)–(.45), we have the following expression

$$y = \frac{\delta}{a_1 k_a Re_a^m Pr_a^{1/3}} + \frac{A_a}{A_w} \frac{D_i}{b_1 k_w Re_w^n Pr_w^{0.3}} \quad (.47)$$

or rewriting the above equation, we have

$$y = c_1 a \alpha^{-m} + c_2 b \beta^{-n} \quad (.48)$$

where $a = 1/a_1$, $b = 1/b_1$, $c_1 = \delta/(k_a Pr_a^{1/3})$, $c_2 = (A_a/A_w)(D_i/k_w Pr_w^{0.3})$ and $\alpha = Re_a$, $\beta = Re_w$.

According to least-squares approach, we require the following expression have its minimum value for proper values of a , b , m and n :

$$S = \sum_{i=1}^{i=N} [y_i - ac_{1i}\alpha_i^{-m} - bc_{2i}\beta_i^{-n}]^2 \quad (.49)$$

which leads to

$$\frac{\partial S}{\partial a} = 0 \quad (.50)$$

$$\frac{\partial S}{\partial b} = 0 \quad (.51)$$

and

$$\frac{\partial S}{\partial m} = 0 \quad (.52)$$

$$\frac{\partial S}{\partial n} = 0 \quad (.53)$$

Then we have

$$a \left[\sum_{i=1}^{i=N} (c_{1i}\alpha_i^{-m})^2 \right] + b \left[\sum_{i=1}^{i=N} c_{1i}c_{2i}\alpha_i^{-m}\beta_i^{-n} \right] = \sum_{i=1}^{i=N} y_i c_{1i}\alpha_i^{-m} \quad (.54)$$

$$a \left[\sum_{i=1}^{i=N} c_{1i}c_{2i}\alpha_i^{-m}\beta_i^{-n} \right] + b \left[\sum_{i=1}^{i=N} (c_{2i}\beta_i^{-n})^2 \right] = \sum_{i=1}^{i=N} y_i c_{2i}\beta_i^{-n} \quad (.55)$$

and

$$a \left[\sum_{i=1}^{i=N} (c_{1i}\alpha_i^{-m})^2 \ln \alpha_i \right] + b \left[\sum_{i=1}^{i=N} c_{1i}c_{2i}\alpha_i^{-m}\beta_i^{-n} \ln \alpha_i \right] = \sum_{i=1}^{i=N} y_i c_{1i}\alpha_i^{-m} \ln \alpha_i \quad (.56)$$

$$a \left[\sum_{i=1}^{i=N} c_{1i}c_{2i}\alpha_i^{-m}\beta_i^{-n} \ln \alpha_i \right] + b \left[\sum_{i=1}^{i=N} (c_{2i}\beta_i^{-n})^2 \ln \beta_i \right] = \sum_{i=1}^{i=N} y_i c_{2i}\beta_i^{-n} \ln \beta_i \quad (.57)$$

So based on experimental data, we can determine y_i , c_{1i} , c_{2i} , α_i and β_i . Then using the equations (.54)–(.57), we can calculate the constants a , b , m and n .

The Fortran program for this purpose can be found in Appendix-3.

APPENDIX-C: FORTRAN CODE

```
double precision lwtc,ewtc,eatc,latc
double precision qw,rew,qa,rea,gpmsi,cfmsi
double precision pi,l,w,d,tl,t,fs,od,id,afr,ata,aca,atw,acw
double precision af,ap,ro,ri,af,afin,roc,tm,tf,gpm
double precision row,muw,kw,cpw,prw,roa,mua,ka,cpa,pra
double precision q,utotal,ga
double precision gpm,ewtc,lwtc,eatc,latc,cfmsi
double precision aa,mm,bb,nn,err1,err2
double precision praa(500),prww(500)
double precision r1(500),r2(500),r3(500),r4(500)
double precision alpha(500),belta(500),c1(500),c2(500),y(500),uc(500)
double precision errrel
double precision fnorm,x(n),xguess(n)
integer i,itn,itmax,n
parameter (n=4)
double precision fnorm,x(n),xguess(n)
external fcn,dneqnf,rnun
common itn
common alpha(500)
common belta(500)
common c1(500)
common c2(500)
```

```
common y(500)
open (1,file='Original-data-All-final.data')
itn=259
call rnun (500,r1)
call rnun (500,r2)
call rnun (500,r3)
call rnun (500,r4)
```

```
*      declaration of all geometric constants for
*      Trane type t coil in cooling mode with 110 fins/ft
```

```
*      l= coil length, m
*      w= coil width, m
*      d= coil depth, m
*      tl= total coil length, m
*      t= fin thickness, m
*      fs= fin space, m
*      od= outer tube diameter, m
*      id= inner tube diameter, m
*      afr= airside frontal area,  $m^2$ 
*      ata= total surface area,  $m^2$ 
*      aca= free airside flow area,  $m^2$ 
*      atw= total waterside surface area,  $m^2$ 
*      acw= free waterside flow area,  $m^2$ 
```

```

pi=4.0*datan(1.0d+0)
l=24.0*(2.54*0.01)
w=18.0*(2.54*0.01)
d=2.0*(2.54*0.01)
tl=290.0*(2.54*0.01)
t=.0050*(2.54*0.01)
fs=(135.0/48.0)*(1.0d-3)
od=.625*(2.54*0.01)
id=.585*(2.54*0.01)
afr=l*w
ata=(d*w*2.0*220.0)+(od*tl*pi)
af=d*w*2.0*220.0
ap=ata-af
aca=afr
acw=(pi*(id/2.))**2.)
atw=pi*id*tl
afin=d*w/12.0
ri=od/2.0
ro=sqrt(afin/pi+ri*ri)
roc=ro+t/2.0
do 10 i=1,itn
read (1,*)gpm,ewtc,lwtc,eatc,latc,cfmsi
gpmsi=gpm*((1.0d-3)/0.2642)/60.0

```

```

tm=0.5*(ewtc+lwtc)+273.15
tf=(tm-273.15+(eatc+latc)/2.)/2.+273.15
call property(tm,tf,row,muw,kw,cpw,prw,roa,mua,ka,cpa,pra)
praa(i)=pra
prww(i)=prw
qw=row*cpw*gpmsi*(ewtc-lwtc)
qa=roa*cpa*cfmsi*(latc-eatc)
q=(qa+qw)/2.0
rew=4.0*gpmsi*row/(pi*id*muw)
ga=roa*cfmsi/aca
rea=fs*ga/(mua)
alpha(i)=rea
belta(i)=rew
utotal=(row*gpmsi*cpw/ata)*dlog((ewtc-eatc)/(lwtc-eatc))
uc(i)=utotal*ata
y(i)=1.0/utotal
c1(i)=fs/(ka*(pra**0.33333))
c2(i)=(ata/atw)*(id/(kw*(prw**0.3)))
10 continue
write(*,*) ”reading data ends ok”, itn
err1=1.0d-2
do 30 i=1,100
xguess(1)=10.0*(1.0+0.05*r1(i))
xguess(2)=0.6*(1.0+0.05*r2(i))

```

```

xguess(3)=0.5*(1.0+0.05*r3(i))
xguess(4)=0.7*(1.0+0.05*r4(i))
errrel = 1.0d-4
itmax = 2000000
call dneqnf (fcn,errrel,n,itmax,xguess,x,fnorm)
write(*,*)(1.0/(x(1)),x(2),(1.0/(100.0*x(3))),x(4),dsqrt(fnorm))
err2=dsqrt(fnorm)
if(err1.lt.err2) goto 30
err1=err2
aa=1.0/(x(1))
mm=x(2)
bb=1.0/(100.0*x(3))
nn=x(4)
30  continue
write(*,*)aa,mm,bb,nn
end

```

————-nonlinear solver subroutine————-

```

subroutine fcn (x,f,n)
integer n,itn,i
double precision x(n),f(n)
double precision a11,a12,a22
double precision alpha(500),beta(500),c1(500),c2(500),y(500)
double precision d1,d2,f01,f02,f03,f04,f11,f12,f21,f22,d1,d2
common itn

```

```

common alpha(500)
common belta(500)
common c1(500)
common c2(500)
common y(500)

intrinsic dlog

a11=0.0d+0
a12=0.0d+0
a22=0.0d+0
d1=0.0d+0
d2=0.0d+0
f01=0.0d+0
f02=0.0d+0
f03=0.0d+0
f04=0.0d+0
f11=0.0d+0
f12=0.0d+0
f21=0.0d+0
f22=0.0d+0

do 100 i=1,itn
a11=a11+c1(i)*c1(i)*(alpha(i)**(-2.0*x(2)))
a12=a12+c1(i)*c2(i)*(alpha(i)**(-x(2)))*(belta(i)**(-x(4)))
a22=a22+c2(i)*c2(i)*(belta(i)**(-2.0*x(4)))
d1=c1(i)*y(i)*(alpha(i)**(-x(2)))+d1

```

```

d2=d2+y(i)*c2(i)*(belta(i)**(-x(4)))
f11=c1(i)*c1(i)*(alpha(i)**(-2.0*x(2)))*dlog(alpha(i))+f11
f12=c1(i)*c2(i)*(alpha(i)**(-x(2)))*(belta(i)**(-x(4)))*dlog(alpha(i))+f12
f01=y(i)*c1(i)*(alpha(i)**(-x(2)))*dlog(alpha(i))+f01
f22=f22+c2(i)*c2(i)*(belta(i)**(-2.0*x(4)))*dlog(belta(i))
f21=f21+c1(i)*c2(i)*(alpha(i)**(-x(2)))*(belta(i)**(-x(4)))*dlog(belta(i))
f02=f02+y(i)*c2(i)*(belta(i)**(-x(4)))*dlog(belta(i))
100  continue
f(1)=a11*x(1)+a12*(100.0*x(3))-d1
f(2)=a12*x(1)+a22*(100.0*x(3))-d2
f(3)=f11*x(1)+f12*(100.0*x(3))-f01
f(4)=f22*(100.0*x(3))+f21*x(1)-f02
return
end
-----property subroutine-----
subroutine property(tm,tf,row,muw,kw,cpw,prw,roa,mua,ka,cpa,pra)
double precision tm,tf,row,muw,kw,cpw,prw,roa,mua,ka,cpa,pra
-----water properties-----
row=754.5+1.87*tm-(3.56d-3)*(tm**2)
muw=0.11-(9.42d-4)*tm+(2.69d-6)*(tm**2)-(2.58d-9)*(tm**3)
kw=-1.09+(9.44d-3)*tm-(1.27d-5)*(tm**2)
cpw=(1.0d+3)*(9.03-(4.04d-2)*tm+(1.10d-4)*(tm**2)-(9.62d-8)*(tm**3))
prw=4340.6-50.47*tm+(2.21d-1)*(tm**2)-(4.30d-4)*(tm**3)
* +(3.14d-7)*(tm**4)

```

————air properties————

$$\text{roa}=4.50-(2.15\text{d-}2)*\text{tf}+(4.56\text{d-}5)*(tf^{**}2)-(3.62\text{d-}8)*(tf^{**}3)$$

$$\text{mua}=(1.0\text{d-}6)*(6.61+0.030*\text{tf}-(3.03\text{d-}5)*(tf^{**}2))$$

$$\text{ka}=(1.0\text{d-}2)*((-2.83\text{d-}1)+(1.17\text{d-}2)*\text{tf}-(6.60\text{d-}6)*(tf^{**}2))$$

$$\text{cpa}=(1.0\text{d+}3)*(1.005)$$

$$\text{pra}=.7674-(2.51\text{d-}4)*\text{tf}+(1.0823\text{d-}7)*(tf^{**}2)$$

return

end